Design optimization of a-Si:H p-i-n, μc-Si:H p-i-n, and micromorph tandem PV cell

by

Nazmul Islam Sarkar
Examination Roll number: 514
Registration number: Ha 218
Admission session: 2014 - 2015

A thesis submitted in partial fulfillment for the degree of
Master of Science
in
Renewable Energy Technology

Institute of Energy
UNIVERSITY OF DHAKA

October 2016

Declarations

Candidate's Declaration:

I confirm that this thesis represents my own work; the contribution of any supervisors and others to the research and to the thesis was consistent with normal supervisory practice. External contributions to the research are acknowledged.

Signed: ______________________________

Date: ______________________________

Supervisor's Declaration:

The MS level research on "Design optimization and study of aSi:H p-i-n, μc-Si:H p-i-n, and micromorph tandem PV cell" has been carried out and the dissertation was prepared under my direct supervision. Hereby I confirm that, to the best of my knowledge the thesis represents the original research work of the candidate; the contribution made to the research by me, by others of the University was consistent with normal supervisory practice, and external contributions to the research are acknowledged.

I believe the thesis to be in a suitable presentational form and is ready for examination.

Signed: ______________________________

(Dr. Himangshu Ranjan Ghosh)
Lecturer
Institute of Energy, University of Dhaka
Dhaka, Bangladesh

Date: ______________________________

Abstract

The performance of a solar cell depends on different design parameters like its doping concentration, layer thicknesses, bandgaps, etc. To ameliorate the solar cell performance studies are done on the effects of different device parameters on its efficiency and others using different solar cell simulation software to skip repeated costly and time consuming experiments in advanced semiconductor labs. In this research, studies on numerical design and performance optimization of a single junction hydrogenated amorphous (a-Si:H) p-i-n cell, hydrogenated single junction microcrystalline (μc-Si:H) p-i-n cell, and micromorph tandem solar cell have been carried out using well-practiced AFORS-HET software. The analyses show that short circuit current density, open circuit voltages, maximum fill factors and the efficiency for the above three configurations cell can be achieved in the range of 10.77 mA/cm^2 to 33 mA/cm^2, 906.5 mV to 1442 mV, 68.9% to 85.3% and 13.26% to 20.78% respectively. These numerically designed cells can perform very well in high frequency spectrum. For lights of 300 to 500 nm wavelengths the external quantum efficiencies (EQE) of micromorph tandem structure and a-Si:H p-i-n cell have high but for 600 to 800 nm wavelengths, its value is low. On the other side for the lower wavelength spectrum the EQE of μc-Si p-i-n is low, but comparatively higher than that of conventional c-Si cell and high for upper wavelength spectrum. The results for short circuit current density of 33 mA/cm^2, open circuit voltage of 906.5 mV, fill factor of 69.4% and efficiency of 20.78% of a hydrogenated single junction microcrystalline (μc-Si:H) p-i-n cell solar cell reveals that it is best and would emulate the performance of other structures shortly.

Acknowledgements

The author wishes to express his deepest gratitude to his supervisor Dr. Himangshu Ranjan Ghosh for his guidance, advice, criticism, encouragements and insight throughout the research.

The author would also like to thank Prof. Dr. Saiful Huque, Director, The Institute of Energy, University of Dhaka, for his suggestions and comments and for providing proper research environment.

The Helmholtz-Zentrum Berlin team is also gratefully acknowledged for providing the AFORS-HET software.

Contents

List of Figures

List of Tables

Abbreviations

A	Cross sectional **A**rea of p-n diode
APCVD	**A**tmospheric **P**ressure **C**hemical **V**apor **D**eposition
BSF	**B**ack **S**urface **F**ield
CVD	**C**hemical **V**apor **D**eposition
Eg	Band Gap
FF	**F**ill **F**actor
h	Plank's Constant
$\mathbf{I}_D$	Junction Current Flow
$\mathbf{I}_L$	Load Current
$\mathbf{I}_o$	Reverse saturation current (dark current)
$\mathbf{I}_{SC}$	Short Circuit current
$\mathbf{J}_{SC}$	Short Circuit Current Density
K	Boltzmann constant
n	Density of Free Electrons
$\mathbf{N}_A$	Acceptor densities
$\mathbf{N}_D$	Donar densities
PECVD	**P**lasma **E**nhanced **C**hemical **V**apor **D**eposition
$\mathbf{V}_{OC}$	Open Circuit Voltage
$\mathbf{P}_{max}$	Maximum Power Output
SWE	**S**taebler-**W**ronski **E**ffect

Chapter 1

Introduction

1.1 Background

The ever-growing energy consumption worldwide along with disastrous effects of fossil fuel burning in the environment is making it essential to find a sustainable solution for the growing energy need. Although solar photovoltaic technology is not the sole answer to this problem but it is one of the most promising technology which has already reach grid parity in some countries and is growing tremendously to achieve grid parity soon in most of the countries [1].

The first solar cell was demonstrated by Ohl in 1941 [2]. After that within last few years the production of PV increased more than 200 times and among them 90% are crystalline silicon (c-Si) based technology [3]. However, c-Si is an indirect bandgap semiconductor which needs a thick layer of wafers to get good amount of current which eventually increases cost of production.

In recent years, the use of hydrogenated amorphous Silicon (a-Si:H) technology advanced rapidly and entered into large scale production and now being sold at lower prices than crystalline silicon (c-Si) modules [4]. This is because of the properties of these materials such as the controllability of their valence electrons, their higher optical absorption coefficient as compared with c-Si semiconductors, their excellent photoconductivity, and possibility of mass-production through large-area non-epitaxial growth on any substrate material. However, compared to crystalline silicon the efficiency of commercially available aSi:H solar cell module are low. While laboratory stabilized efficiencies over 10%

have been demonstrated for small size cells, there is a gap between this record test cells and the translation into commercial modules [5]. It is interesting to look into the various individual factors that cause efficiency losses for aSi:H technology between laboratory records cell and industrial production [6].

Hydrogenated microcrystalline silicon (μc-Si:H) films are also being widely used and has replaced amorphous silicon due to its better stability and higher conductivity under illumination [7]. Vepvrek et al. [8] first introduced the use of hydrogenated microcrystalline silicon. Nowadays it is generally obtained from PECVD process using a mixture of silane and hydrogen [9]. It is a kind of material which combines the advantages of amorphous silicon (a-Si:H) with higher stability and long wavelength spectral sensitivity of crystalline silicon [10]. Initially, Faraji et al. [11] prepared hydrogenated and oxygenated microcrystalline silicon (μc-Si:O:H) by RF glow discharge with a mixture of silane, hydrogen, and oxygen and used it as i layer of a p-i-n configuration which depicted 7.8% efficiency. Later on, many researchers developed stable μc-Si:H solar cells using various fabrication processes [12, 13]. Microcrystalline silicon is a biphasic material with microcystallities embedded in amorphous material [14]. It is also an indirect bandgap semiconductor which requires a thick intrinsic layer in a p-i-n cell [15]. Microcrystalline silicon can be deposited in large area and is low cost as in the case of amorphous silicon but with higher stability [16].

As third generation photovoltaic devices tandem cells achieve higher efficiencies than that of single junction solar cells [17]. Thin film amorphous single junction solar cell has higher bandgap, ability to absorb the high energy photons and are cost effective [18]. On the other hand, its micro-crystalline counterpart has lower bandgap which can absorb low energy photons and can also be deposited in large area and thus has low cost production process [16]. However, both amorphous and microcrystalline suffer from lower efficiency and lower stability at outdoor conditions. Therefore, the idea of tandem structure of amorphous and microcrystalline junctions got popular which has better spectrum utilization and better stability with higher efficiency. This tandem structure of hydrogenated amorphous silicon (a-Si:H) p-i-n cell and hydrogenated microcrystalline silicon (μc-Si:H) p-i-n cell is often called as micromorph cell. Usually, PECVD or hot wire processes are used to deposit the thin film layers of micromorph cell directly on glass substrate [19].

1.2 Objectives

The objectives of this thesis are to study the single junction hydrogenated amorphous silicon (a-Si:H), single junction hydrogenated microcrystalline silicon (μc-Si:H), and tandem structure of micromorph solar cell where a-Si:H p-i-n cell is used as the top cell and μc-Si:H p-i-n cell is used as the bottom cell. The optimization of single junction a-Si:H p-i-n cell, single junction μc-Si:H p-i-n cell, and their tandem structure is also done using numerical simulation tool AFORS-HET. In brief, the objectives of the research are:

• To study the modeling of solar cells along with their equivalent circuit, and finding out the effect of model parameters.

• To design and analyze the thin film single junction hydrogenated amorphous silicon (aSi:H) p-i-n device and optimize its performance by tuning of its various parameters.

• To design, analyze, and optimize the thin film single junction hydrogenated microcrystalline silicon (μc-Si:H) p-i-n device.

• To study, analyze and find the optimum structure of micromorph tandem solar cell.

1.3 Chapter contents

The rest of the thesis is organized as follows:

Chapter 2 describes the important material parameters of crystalline silicon, amorphous silicon, and both a-Si:H and μc-Si:H materials.

Chapter 3 discusses the stability and degradation of a-Si:H p-i-n cell, μc-Si:H p-i-n cell, and micromorph tandem cell.

Chapter 4 elaborates the working principles of a PV cell and its various models and equivalent circuits and also analyzes the effects of model parameters on the simulation of PV cell. OrCAD PSPICE is used to analyze and simulate the effects of parameters on photovoltaic cell performance.

Chapter 5 illustrates the design and analysis of thin film single junction hydrogenated amorphous silicon (aSi:H) p-i-n device and also details the procedure to optimize its performance. This part of the research has been carried out with AFORS-HET modeling and computer simulation program.

Chapter 6 studies the design optimization and analysis of thin film single junction hydrogenated microcrystalline silicon (μc-Si:H) p-i-n device.

Chapter 7 studies the design optimization and analysis of micromorph tandem solar cell.

Chapter 8 concludes the thesis with comparison and summary of all results and outcomes.

Chapter 2

Material Parameters

Various materials are being used for solar cell preparation among which mono-crystalline and poly-crystalline silicon are the most used and available in the market. For thin-film preparation amorphous silicon, micro- or nano-crystalline silicon is used. Besides these, Cadmium Telluride cells, Copper indium gallium selenide solar cells (CIGS), or Gallium arsenide germanium solar cell (GaAs) are there which are made from various photovoltaic materials. However, as this study is limited within the amorphous and crystalline form of silicon, the material parameters of these two types will be studied.

2.1 Crystalline Silicon

Crystalline Silicon can be of three types depending on the manufacturing process namely:
(i) Mono-crystalline Silicon,
(ii) Poly- or Multi-crystalline Silicon, and
(iii) Micro- or Nano-crystalline silicon.

In the following subsections the materials parameter of these types are discussed.

2.1.1 Mono-crystalline Silicon

Mono-crystalline silicon is an indirect bandgap semiconductor [20]. The crystal structure of mono-crystalline silicon is arranged in the form of two interwoven face-centered cubic lattices with one silicon atom placed on each lattice point as shown in figure 2.1[21].

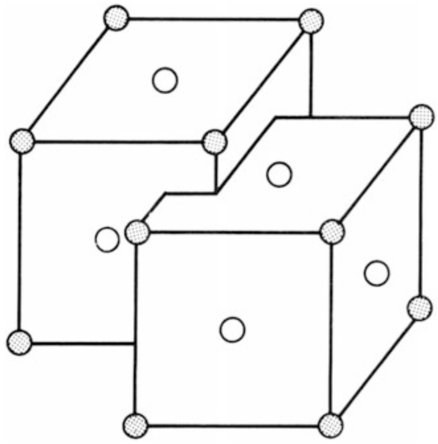

FIGURE 2.1: Crystal lattice structure of Silicon

The bonds in crystalline silicon are purely covalent. The two elementary cells are displaced against each other by a quarter of the body diagonal. Figure 2.2 shows the absorption coefficient of mono-crystalline silicon at room temperature [22].

In Table 2.1 the crystal properties of silicon along with thermal, dielectric, and electric properties are given. Room temperature (300 K) is assumed for the temperature dependent characteristics such as thermal conductivity and dielectric properties [21, 23].

Some electric properties such as electron affinity, breakdown voltage, and drift velocity depend on doping or impurity levels so that typical values can be given only.

2.1.2 Multi-crystalline Silicon

Multicrystalline (polycrystalline) silicon consists of monocrystalline grains, which are randomly oriented. The grains have sizes of some micrometer up to some centimeter and are confined by grain boundaries, regions of unfavorable electrical properties. Table 2.2 gives Some material properties of poly-crystalline silicon [24].

2.1.3 Micro-crystalline Silicon

Microcrystalline silicon (μc-Si:H), is a material, which consists of crystallites with diameters between 1 and 100 nm. They are separated either by grain boundaries or by amorphous silicon. The electrical and optical properties of this material differ strongly from those of the monocrystalline, polycrystalline, or amorphous phases [24, 25].

TABLE 2.1: Some material properties of crystalline silicon

Properties	Values
Crystal properties	
Atoms/cm^{-3}	5.0×10^{22}
Atomic weight	28.09
Density (g/cm^3)	2.24
Melting point (°C)	1,415
Vapor pressure (Pa)	1 at 1,650 °C, 10^{-6} at 900 °C
Thermal properties	
Coefficient of thermal expansion (°C^{-1})	2.6×10^{-6}
Specific heat (J/g × °C)	0.7
Thermal conductivity (W/cm × °C)	1.5
Thermal diffusion coefïňĄcient (cm^2/s)	0.9
Dielectric properties	
Dielectric constant	11.9
Electric properties	
Bandgap (eV)	1.12
Intrinsic carrier concentration (cm^{-3})	1×10^{10}
Intrinsic Debye length (μ m)	24
Intrinsic speciïňĄc resistivity (Ω cm)	2.3×10^5
Effective state density in the conductance band, $N_c(cm^{-3})$	2.8×10^{19}
Effective state density in the valence band, $N_v(cm^{-3})$	1.04×10^{19}
Electron afïňĄnity, χ (V)	4.05
Breakdown voltage (V/cm)	$\approx 3 \times 10^5$
Minority carrier lifetime (s) (intrinsic material)	2.5×10^{-3}
Drift mobility ($cm^2/V \times s$) electrons/holes	1500/450

TABLE 2.2: Some material properties of poly-crystalline silicon

Properties	Values
Electric properties	
Specific resistivity (Ω cm)	4×10^5 (doping level $< 10^{15} cm^{-3}$)
Minority carrier lifetime (s)	8×10^{-11}, grain size 0.2 μm, $7 \times 10 - 6$, grain size 4,000 μm
Drift mobility ($cm^2/V \times s$), electrons	40
Optical properties	
Effective refractive index	3.93 after deposition at T $<$ 580 °C, 3.51 after deposition at T $>$ 600 °C

Microcrystalline silicon is produced with the same setups as the amorphous hydrogen-rich material. During a-Si:H production, a small portion of the deposited film is always produced in microcrystalline form. As a rule, this contribution is negligible. However, for

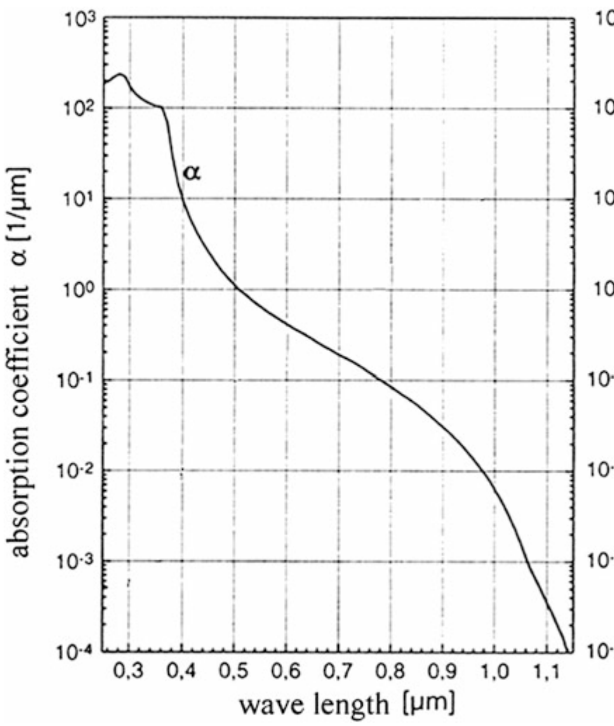

FIGURE 2.2: Absorption coeffcient, α with respect to wavelength, λ at room temperature

TABLE 2.3: Some material properties of micro-crystalline silicon

Optical properties	Values
Index of refraction	4.05 at 500 nm
Optical band gap (eV)	1.6 at 210 °C substrate temperature
	2.0 at 350 °C substrate temperature
Absorption coefiňĄcient (cm^{-1}) at 3.5 eV	5.82×10^6

appropriate process parameters, the overwhelming majority of the film will appear as μc-Si:H. A typical example is the formation of the film in a plasma-enhanced chemical vapor deposition (PECVD) setup, where the silane is highly diluted in hydrogen. The latter acts as an etching gas for the amorphous phase so that the microcrystalline component is left over. Table 2.3 shows some properties of μc-Si:H material [25, 26].

2.2 Hydrogenated Amorphous Silicon

Crystalline silicon (c-Si) can be designated as 4-fold coordinated network, where one silicon atom is tetrahedrally bonded to four neighboring silicon atoms. This tetrahedral structure is continued, forming a well-ordered lattice (crystal). In contrary, within amorphous silicon (a-Si), not all the atoms are 4-fold coordinated due to a continuous random

TABLE 2.4: Material properties of hydrogenated amorphous silicon

Properties	Values
Optical properties	
Bandgap (eV)	1.4 - 1.9
Material properties	
Hydrogen content (%), typical	10 - 30
Density (g/cm^3) for two hydrogen concentrations	2,20 at 10 % hydrogen content
	2,11 at 20 % hydrogen content
Dielectric properties	
Dielectric constant for two hydrogen concentrations, N_H	14 at $N_H = 5 \times 10^{21} cm^{-3}$
	6 at $N_H = 17 \times 10^{21} cm^{-3}$
Electric properties (typical)	
Intrinsic specific resistivity (Ω cm)	2×10^{10} at room temperature
Maximum specific conductivity after doping (Ω cm)	10^{-2} at room temperature
Effective state density at the conduction band edge, $N_c(cm^{-3})$	4.5×10^{21}
Effective state density at the valence band edge, $N_v(cm^{-3})$	6.4×10^{21}
State density at midgap (cm^{-3})	$10^{17} - 10^{18}$
Recombination lifetime (s)	$10^{-9} - 10^{-2}$
Drift mobility (cm^2/Vs) electrons/holes	1/0.01

network. Due to the disordered nature of the amorphous silicon, some atoms feature an unsaturated band ("dangling bond") (db). These dangling bonds can be described as broken covalent bonds, which are also found on the surface of crystalline silicon due to the absence of lattice atoms above them. The amorphous character yields either a neutral, positive, or negative charge of the db. As a result, once a metal is deposited on a silicon surface, these dangling bonds rise to interface states within the energy bandgap of silicon. If desired, the material can be passivated by hydrogen. Additional hydrogen bonds to the db and can reduce the db density by several orders of magnitude. Table 2.4 shows some of the material properties of a-Si:H material [3, 27].

Chapter 3

Stability and Degradation of Solar Cell

3.1 Staebler-Wronski effect

Amorphous silicon layers suffer from light induced degradation that is under the influence of light exposure amorphous silicon layers show a pronounced increase in dangling bond density by about 1 to 2 orders of magnitude, before they finally more or less stabilize, after some 1000 hours of light exposure. This phenomenon is known as the "Staebler-Wronski effect (SWE)".

The defect density of hydrogenated amorphous silicon (a-Si:H) increases with light exposure, causing an increase in the recombination current and reducing the efficiency of the conversion of sunlight into electricity.

It was discovered by David L. Staebler and Christopher R. Wronski in 1977. They showed that the dark current and photoconductivity of hydrogenated amorphous silicon can be reduced significantly by prolonged illumination with intense light. However, on heating the samples to above 150 °C, they could reverse the effect [29].

The exact nature and cause of the SWE is still not well known. Microcrystalline silicon suffers less from the Staebler-Wronski effect than amorphous silicon, suggesting that the disorder in the amorphous silicon Si network plays a major role. Other properties that could play a role are hydrogen concentration and its complex bonding mechanism, as well as the concentration of impurities.

Now, dangling bonds act as recombination centers, so that an increased dangling bond density results in reduced drift lengths. It also means, for the pin-solar cell, an increased space charge within the i-layer, due to charged dangling bonds, especially due to negatively charged dangling bonds near the n/i-interface. This leads to a deformation/reduction in the internal electric field and again to a decreased drift length. It is therefore evident that amorphous silicon solar cells will also be affected by light-induced degradation and that their conversion efficiency will be reduced, especially in the case of thick cells.

In amorphous silicon solar cells, light-induced degradation mainly affects the fill factor and, usually to a lesser extent, the short-circuit current J_{SC}; it has, in general, a very limited effect on the open circuit voltage V_{OC}. Physically, light-induced degradation is caused by the recombination of carriers within the cell; it is therefore much stronger when the cell is open-circuited, i.e. when the internal field is strongly reduced, and is still substantial when the cell is operated with a load resistance close to the maximum power point. Under short-circuit conditions, the internal field is larger, and hence the recombination and resulting degradation are weaker.

Furthermore, light-induced degradation is a reversible effect; cells can be annealed by heating them for a few hours, to around 150 ÂřC, where they attain their initial efficiency again. In a very simple model, one can view the actual process always as equilibrium between a degradation component (i.e. the creation of additional dangling bonds) and an annealing component (i.e. the suppression or "healing" of dangling bonds). For this reason degradation is more severe (and stabilized efficiency values reached are lower) when the operating temperature is lower.

In practice, for present state-of-the-art amorphous silicon solar cells one finds a degradation of around 10% to 30% for cells with i-layer thicknesses between 200 nm and 400 nm; cells with thicker i-layers have higher relative degradation, however, i-layer thickness is not the only factor involved. Unfortunately, the short-circuit current density J_{SC} decreases with decreasing i-layer thickness, so that a compromise has to be found. With present methods of light trapping the optimal i-layer thickness is somewhere around 200 to 250 nm.

3.2 Methods for reducing Staebler-Wronski effect

In spite of a huge research effort, so far no method has been found to avoid the Staebler-Wronski effect. However, the effect can be somewhat reduced by using a moderate amount of hydrogen dilution during plasma deposition of the amorphous layer. Microcrystalline silicon solar cells only show a very mild form of light-induced degradation. The extent of degradation observed depends on the crystalline volume fraction: hydrogenated microcrystalline silicon is a "mixture" of an amorphous matrix and of crystallites. The best cells so far fabricated have a crystalline volume fraction of around 60 to 70%. These cells show a relative efficiency degradation of 5% or less, even when their i-layer is 2 Îijm thick [30, 31].

The use of tandem and multi-junction solar cells is one way to reduce the effect of light -induced degradation: the top cell in a tandem can be kept very thin and, therefore shows little light-induced degradation; the bottom cell is not exposed to the full AM 1.5 spectrum and therefore shows once again less light-induced degradation. In fact, for a "micromorph" (microcrystalline/amorphous) tandem structure, no light-induced degradation whatsoever has been observed in the microcrystalline bottom cell [14].

3.3 Defect states and Dangling bonds in Amorphous Silicon

Ionized defects (charged dangling bonds) have a charge state that is "amphoteric", i.e. it can take on both charge signs, and be either positively or negatively charged. They become charged by capturing free holes or free electrons; their charge state is, thus, governed by the ratio pf(x): nf(x).

Intuitively one can visualize the following behavior:

• if the density of free holes is much larger than the density of free electrons, the dangling bonds will be mainly positively charged, because they can easily capture a free hole but have to wait a long time before capturing one of the scarce free electrons;

• on the other hand, if the density of free electrons is much larger than the density of free holes, the dangling bonds will be mainly negatively charged;

• and, finally, if the densities of both carriers are in the same range, the dangling bonds will be mainly neutral.

To calculate the occupation functions for the three charge states one has to look in detail at the capture processes. The procedure is similar to that used for "classical" Schockley-Read-Hall (SRH) recombination theory [28]. Just as in the "classical" case, we may also assume for amorphous silicon that:

• the capture rates for electrons are proportional to the density of free electrons that can be captured;

• the capture rates for holes are proportional to the density of free holes that can be captured;

• free electrons have a mobility (μn) 0 that is about 1 to 3 times higher than the mobility of holes (μp) 0 of free holes pf; thus, they have a thermal velocity that is 1 to 3 times higher than the thermal velocity of free holes, and are therefore also about 1 to 3 times more likely to be captured for otherwise comparable parameters.

Chapter 4

Working Principle and Modeling of Solar Cell

Photovoltaic (PV) cell generates electricity when it is illuminated by the sun or some other light sources. Small PV cells can be grouped to form panels and panels can be grouped to form arrays. The tremendous growth of PV industry and the increased number of installed PV systems all over the world raised the need for supervision and simulation tools for PV systems. To understand the PV system in a better way, modeling the PV system in various operating and weather conditions is necessary [32, 33]. The simulation is also useful for various purposes like: (1) to analyze and study the behavior of power converters when they are attached with the PV system, [34, 35] (2) to simulate the behavior of Maximum Power Point Tracker (MPPT), [36, 37] and (3) to estimate the efficiency of the PV system [38, 39]. In addition to these, the simulation can also be used to analyze various operational conditions like: partial shading, change in irradiance, and fault conditions [40, 41].

On the other hand, Manufacturers of the PV modules provide electrical parameters only at standard test conditions (STC) which is at $irradiance = 1000W/m^2$, 1.5 Air Mass (AM), and cell temperature of $T_{cell} = 25°C$ [32]. Manufacturers data sheet only provides the short-circuit current I_{SC}, Open-circuit voltage V_{OC}, the voltage at maximum power point V_{MP}, the current at maximum power point I_{MP} and the temperature coefficients at open-circuit voltage and short-circuit current [42]. However, the operating range of the PV panel is large and operating and weather conditions also vary. Therefore, performance models are built to predict the performance of the PV system at any operating and weather condition. The model predicts the I-V characteristic of a PV system as a function of irradiance, angle of incidence of solar radiation, the spectrum of sunlight, and temperature [43]. For the last few years substantial amount of work has been done to develop simulation models and extraction of model parameters of photovoltaic systems [44–49]. Specially, Ma et al. [50] have developed a model to simulate the performance characteristics of crystalline silicon photovoltaic modules/strings/arrays. Zeroual et al. [51] designed and constructed a closed loop sun-tracker with microprocessor management. Chin et al. [52] have done a design, modeling and testing of standalone single axis active solar tracker using MATLAB/Simulink. Chin [53] has also done model-based simulation of an intelligent microprocessor-based standalone solar tracking system. Models for numerical device simulations of crystalline silicon solar cells was also reviewed by Altermatt [54]. De Blas et al. [55] found suitable models for characterizing photovoltaic devices. Celik and Acikgoz [56] have done the modeling and experimental verification of the operating current of mono-crystalline photovoltaic modules using four- and five-parameter models. Chatterjee et al. [43] have identified suitable photovoltaic source models. However, the effects of individual model parameters were not clearly reviewed in present literature.

The objective of the work in this chapter is to analyze the effects of model parameters on the simulation of PV cell. PSPICE is used to analyze and simulate the effects of parameters on photovoltaic cell performance.

4.1 Working Principle of a PV cell

A photovoltaic cell is usually a semiconductor device that convert sunlight into electricity by the means of photovoltaic effect[57]. When light falls on a solar cell, the incoming photons can be absorbed, reflected or passed through it. For a photon to be absorbed by the solar cell, the energy of the photon must be greater than the band gap energy of the cell [58]. The photon is then absorbed to generate pairs of mobile charge carriers (for example: electron and hole) which are then separated by the structure of the device (such as a p-n junction). This produces a potential difference and thus produce electrical current. The photovoltaic effect is shown by various materials. In most of the cases,

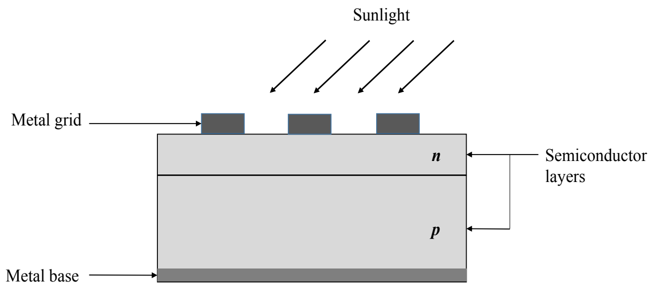

FIGURE 4.1: Photovoltaic cell structure

semiconductor materials (like silicon) in the form of p-n junction are commercially used to produce solar cells [59]. The I-V characteristic of a p-n junction diode is given by the Shockley equation as [58]:

$$I_D = I_0 \left[exp\left(\frac{qV_D}{nkT_{cell}} \right) - 1 \right] \tag{4.1}$$

where, I_D is the current generated by the diode, V_D is the voltage across the diode, I_0 is the reverse saturation current of the diode, $q = 1.602 \times 10^{19}$ Coulombs is the electron charge, T_{cell} is the cell temperature in Kelvin, n is the diode ideality factor (dimensionless), and $k = 1.38065 \times 10^{23} J/K$ is the Boltzmann constant. The reciprocal term of (q/nkT_{cell}) is called the thermal voltage of the diode. Therefore, thermal voltage of the diode is:

$$V_T = \frac{nkT_{cell}}{q} \tag{4.2}$$

Now equation (2.1) becomes:

$$I_D = I_0 \left[exp\left(\frac{V_D}{V_T} \right) - 1 \right] \tag{4.3}$$

The Fill factor of a solar cell is given as:

$$FF = \frac{V_{MPP} I_{MPP}}{V_{oc} I_{sc}} \tag{4.4}$$

A semiconductor p-n junction can be made to operate as a solar cell. Figure 4.1 shows the basic structure of a PV cell. When light is incident on the cell, the photons of light generate free electron-hole pairs which are then attracted toward the junction. Figure

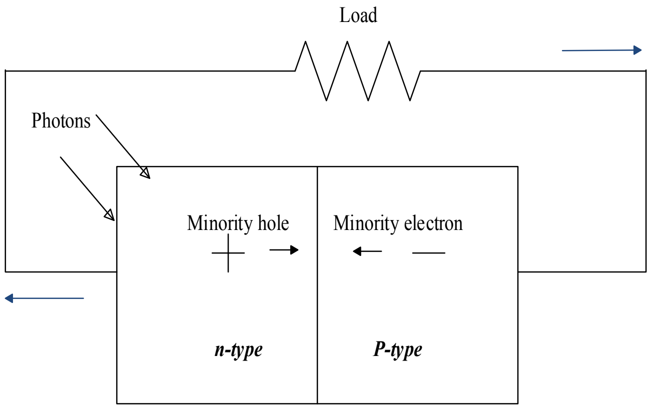

FIGURE 4.2: Photovoltaic cell operation

TABLE 4.1: Model parameters of different models

Models	No. of parameters	Parameters	Parameter Meanings
Ideal single diode model	3	I_L, I_{01}, n_1	I_L, the photocurrent
Single diode R_s model	4	I_L, I_{01}, n_1, R_s	I_{01}, the reverse saturation current of the first diode
Single diode Rp model	5	I_L, I_{01}, n_1, R_s, R_p	I_{02}, the reverse saturation current of the second diode
Two diode model	7	I_L, I_{01}, I_{02}, n_1,n_2, R_s, R_p	I_{03}, the reverse saturation current of the third diode
Three diode model	9	I_L, I_{01}, I_{02}, I_{03}, n_1, n_2,n_3, R_s, R_p	n_1, the first diode ideality factor
			n_2, the second diode ideality factor
			n_3, the third diode ideality factor
			R_s, lumped series resistance
			R_p, shunt resistance

4.2 illustrates the operation of the solar cell. In the cell, electron flows from n-type silicon to p-type silicon. The generated current is proportional to the light intensity [57].

4.2 Modeling of a solar cell

There are various electrical circuit models of photovoltaic cells which have been widely described in the literature [60–63]. Usually, a PV cell is represented by a current source (I_{ph}), one or two diodes (D) in parallel with the current source, a series resistance (R_S) or a parallel resistance (R_p) or both connected. The datasheet of a PV panel provided by the manufacturer usually include few electrical and thermal parameters as given in Table 4.1. All these values are measured at standard test condition which is at 1.5 air mass (AM), 1000 W/m^2, and 25 °C temperature. Usually, the models are known by the unknown number of values of the parameters which can not be deduced directly from datasheet values. In the preceding section, the models and their associated parameters are described.

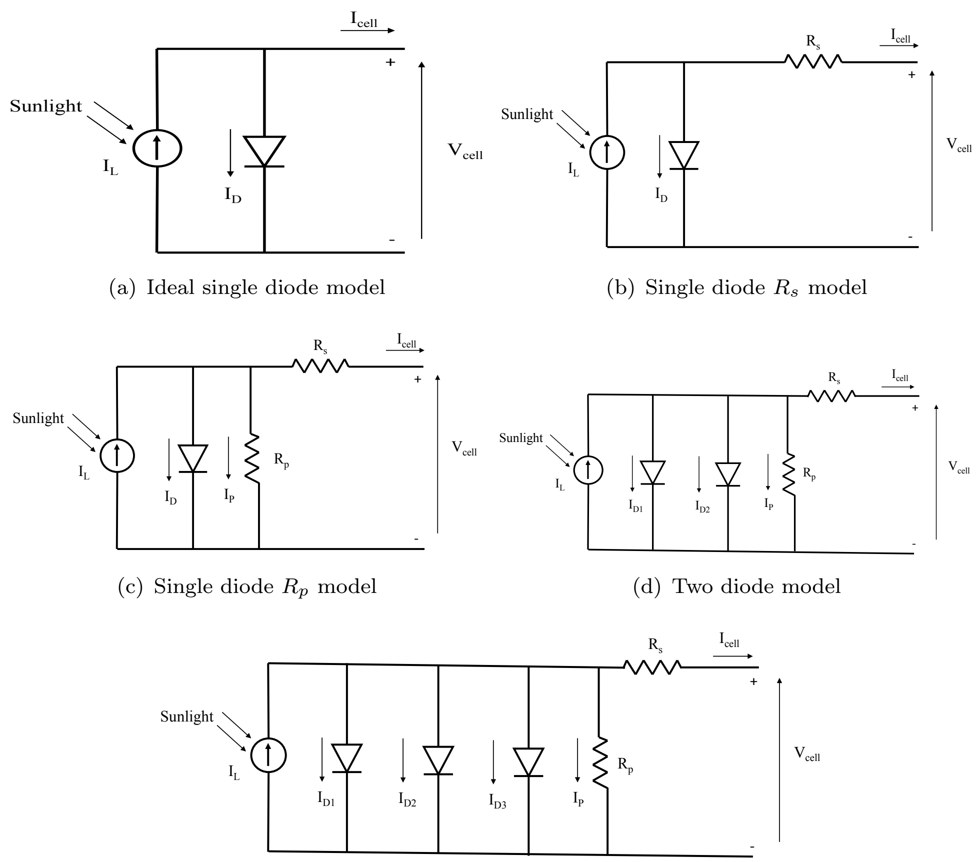

(a) Ideal single diode model

(b) Single diode R_s model

(c) Single diode R_p model

(d) Two diode model

(e) Three diode model

FIGURE 4.3: (a) Ideal Single Diode model, (b) Single Diode R_s model, (c) Single Diode R_p model, (d) Two Diode model, and (e) Three Diode Model of PV cell

TABLE 4.2: Electrical and Thermal parameters available from manufacturer data sheet

Parameters	**Symbol [Unit]**
Electrical Parameters	
Maximum Power Rating	P_{max} $[W_p]$
Rated Current	I_{MPP} [A]
Rated Voltage	V_{MPP} [V]
Short Circuit Current	I_{sc} [A]
Open Circuit Voltage	V_{oc} [V]
Thermal Parameters	
Normal Operating Cell Temperature	NOCT [°C]
Temperature Co-efficient: Short Circuit Current	[A / °C]
Temperature Co-efficient: Open Circuit Voltage	[V / °C]
Standard Test Conditions (STC)	
Air Mass	$AM = 1.5$
Irradiance	$G = 1000W/m^2$
Cell Temperature	$T_{cell} = 25°C$

4.2.1 Ideal cell model

In ideal condition, the solar cell is electrically equivalent to a current source in parallel with a diode as shown in fig. 2.3(a). The light generated current, also known as photocurrent, is represented as I_L, the diode current as I_D, the net current and terminal voltage of solar cell as I_{cell} and V_{cell}, respectively. The net current I_{cell} available from the PV cell is given as:

$$I_{cell} = I_L - I_D \tag{4.5}$$

Substituting the value of I_D from equation (2.3) into equation (2.4) we get:

$$I_{cell} = I_L - I_0 \left[exp\left(\frac{V_{cell}}{V_T}\right) - 1 \right] \tag{4.6}$$

The photocurrent I_L increases linearly with solar insolation. If diode current I_D is small, more current is delivered by the PV cell. The diode ideality factor n indicates how closely the diode follows the ideal diode equation [57]. The value of n greater than 1 represents non-ideal condition, whereas $n = 1$ represents ideal behavior of the diode.

As we can see from equation (2.3) the ideal cell model has 3 parameters to find which are photocurrent I_L, dark current I_0, and diode ideality factor A. Therefore, this ideal model is also called the 3-p (3 parameter) model as shown in Table 4.2. This ideal cell model can be used to demonstrate the basic concept of PV cell but is never used to simulate the actual operating conditions. This is because there are several limitations present in a practical PV cell [47]. The series resistive losses, the shunt resistive losses, the recombination at the space charge region of solar cells which is non-ohmic, and the non-ideality of the diffusion diode all indicate that ideal single diode model is insufficient to accurately represent the maximum power delivered by the PV cell [58].

4.2.2 Single diode R_s model

In fact, the current generated in the photovoltaic cell travels through semiconductor material which are not heavily doped and thus show resistivity [45, 64]. Besides this, the resistance of the metal grid, contacts and current collecting wires also contribute to the total series resistive losses. Usually, a lumped resistor, R_s is added in series with

Table 4.3: Electrical and thermal parameters of SM50 module

Electrical parameters		
Maximum power rating, P_{max}	[Wp]	50
Rated current I_{MPP}	[A]	3.05
Rated voltage V_{MPP}	[V]	16.6
Short circuit current I_{SC}	[A]	3.4
Open circuit voltage V_{OC}	[V]	21.4
Thermal parameters		
NOCT	[°C]	45 ± 2
Temp. coefficient: short-circuit current		1.2 mA / °C
Temp. coefficient: open-circuit voltage		-0.077 V / °C

the ideal circuit model to represent these series losses as shown in fig. 2.3(b) [45]. This model is called single diode R_s model.

Because of the addition of the lumped series resistor, R_s the net current flow through the cell, I_{cell} now becomes:

$$I_{cell} = I_L - I_D \tag{4.7}$$

$$I_{cell} = I_L - I_0 \left[exp\left(\frac{V_{cell} + I_{cell}R_s}{V_T} \right) - 1 \right] \tag{4.8}$$

From equation (2.4) it can be seen that there are now 4 unknown parameters: photocurrent I_L, reverse saturation current I_0, diode ideality factor A, and the newly added lumped series resistor R_s. This model is therefore named as 4-p model. However, in recent research it is shown that the 4-p model which ignores the shunt resistance effect does not perfectly fit the experimental I-V and P-V data [65].

4.2.3 Single diode R_p model

As the solar cells are made out of large area wafers, or from large area thin film material, a number of shunt resistive losses occur at n layer of the $p-n$ junction PV cell. Localized short circuit or short circuiting of the cell border are the most common form of shunt losses [47]. This is represented generally by a lumped resistor, R_{sh}, in parallel with the ideal device. The single diode R_p model which has both the series resistance R_s and shunt resistance R_p is shown in fig. 2.3(c). As there are 5 unknown parameters in this model it is called the 5-p model. Table 4.2, illustrates the models along with their parameters. The current through the parallel resistor, I_P can be given as:

$$I_P = \frac{(V_{cell} + IR_s)}{R_p} \tag{4.9}$$

The governing equation of this 5-p model now becomes:

$$I_{cell} = I_L - I_D - I_P \tag{4.10}$$

$$I_{cell} = I_L - I_0 \left[exp\left(\frac{V_{cell} + I_{cell}R_s}{V_T} \right) - 1 \right] - \frac{(V_{cell} + IR_s)}{R_p} \tag{4.11}$$

This single diode R_p model or 5-p model is the most widely used and accepted model found in the literature [40, 41, 43, 66–70]. Most of the research has been done on the improvement 5-p model and its parameter (I_L,I_0,V_T,R_s,R_p) extraction procedure [32, 40–43, 46, 63].

4.2.4 Two diode model

Even though, the commonly used 5-p model can achieve acceptable level of accuracy, but in fact, the saturation current of the photovoltaic cell is the linear superposition of charge diffusion and recombination in the space-charge layer [58]. Therefore the more accurate electrical representation of the PV cell can be done by two Shockley diodes in parallel with a current source and associated series and shunt resistances [47]. This model is more relevant at low voltage bias i.e. at low irradiance level operation of the PV cell [58]. Figure 4.3(d) illustrates the circuit of this model.

The equivalent circuit equation of the two diode model is given as:

$$I_{cell} = I_L - I_{D1} - I_{D2} - I_P \tag{4.12}$$

$$\begin{aligned} I_{cell} = I_L - I_{01} \left[exp\left(\frac{V_{cell} + I_{cell}R_s}{V_{T1}} \right) - 1 \right] \\ -I_{02} \left[exp\left(\frac{V_{cell} + I_{cell}R_s}{V_{T2}} \right) - 1 \right] - \frac{(V_{cell} + IR_s)}{R_p} \end{aligned} \tag{4.13}$$

We can see form Table 4.2, the number of parameters are increased to 7 in two diode model. To reduce the number of unknowns the ideality factor of the first diode is usually taken as 1 and the second diode ideality factor is taken as 2. This assumption is done based on the approximation of Schokley-Read-Hall recombination in the space charge layer of the photodiode [71]. Unfortunately, this assumption does not always hold true [72].

4.2.5 Three diode model

To take the influence of grain boundaries and leakage current through the peripheries into consideration another diode can be added in parallel with the two other diodes of the two diode model [73]. This model has 9 parameters (see Table 4.2) and a really cumbersome solution process. Most of the time, ignoring few parameters are done to reduce the number of equations of this model. Figure 4.3(e) shows the circuit diagram of this model.

The equation of the current of this model is:

$$I_{cell} = I_L - I_{D1} - I_{D2} - I_{D3} - I_P \tag{4.14}$$

$$\begin{aligned} I_{cell} = I_L - I_{01}\left[exp\left(\frac{V_{cell} + I_{cell}R_s}{V_{T1}}\right) - 1\right] \\ -I_{02}\left[exp\left(\frac{V_{cell} + I_{cell}R_s}{V_{T2}}\right) - 1\right] \\ -I_{03}\left[exp\left(\frac{V_{cell} + I_{cell}R_s}{V_{T3}}\right) - 1\right] - \frac{(V_{cell} + IR_s)}{R_p} \end{aligned} \tag{4.15}$$

This model is usually used to extract the electrical properties of multi-crystalline Si solar cells. Because of the complexity of the parameter extraction process of three diode model, the use of this model is quite limited [45].

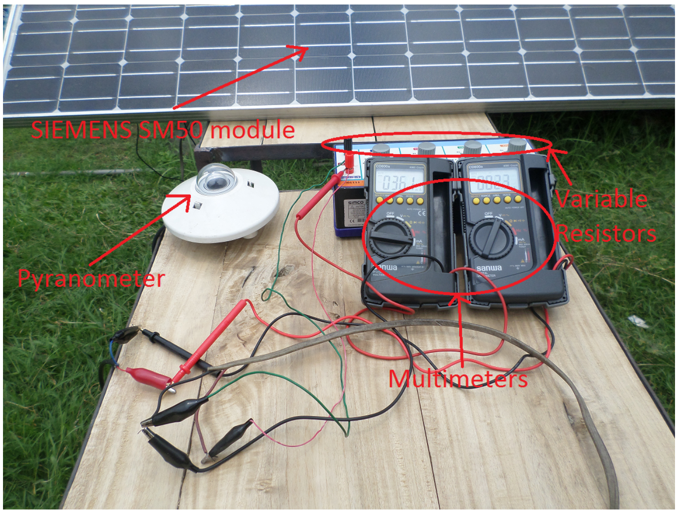

FIGURE 4.4: Experimental Setup with Siemens SM50 module

4.3 Experimental Setup

Siemens SM50 module is connected in series with variable resistors and current and voltages are measured for varying parameters. An Eppley PSP pyranometer is used to take the radiation measurement. The pyranometer gives output in a range of 0-10 mV having sensitivity of approximately $8\mu V/Wm^{-2}$. The SM50 module has 36 mono-crystalline silicon solar cells. The electrical and thermal parameters of this module are enlisted in Table 4.3. Two digital multimeter is used to take current and voltage measurements. Figure 4.4 shows the experimental setup.

4.4 Results and Discussion

Simulation Program with Integrated Circuit Emphasis or SPICE is an open source circuit simulator developed by Nagel and Pederson of University of California, Berkeley in 1973 [74]. With time SPICE became popular and adopted by various institutions. Several proprietary software tool gradually evolved from the basic SPICE. Cadence OrCAD PSPICE is a similar proprietary software tool used to simulate circuit using SPICE. In this study, we have simulated the parameters shown in Table 4.2 to check their effects on the PV system performance. For this purpose we have taken a hypothetical small PV cell with an area of 5 sq. inch, short circuit current density 34.3 mA/cm^2, and dark current I_0 as $10^{-11}A/cm^2$. Using a PSPICE function named PROBE we got the simulation curves. The schematic diagram of the simulation is given in Figure 4.5.

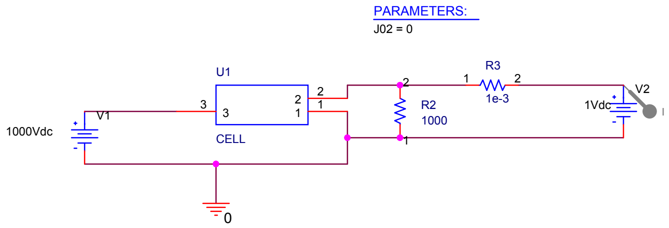

FIGURE 4.5: Schematic diagram of PV cell simulation in PSPICE

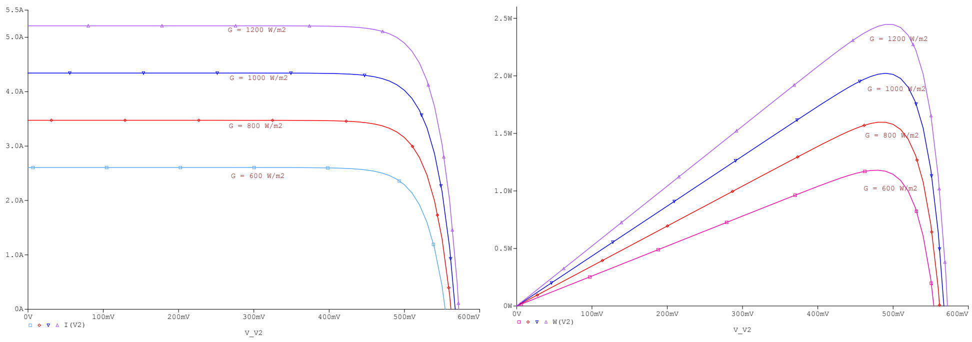

(a) I-V curves with varying irradiance (b) Power curves with varying irradiance

FIGURE 4.6: (a) I-V curves, and (b) Power curves with varying irradiance

4.4.1 Effect of photocurrent, I_L:

The photocurrent I_L is directly proportional to the irradiance received by the PV cell. The value of I_L can be calculated as:

$$I_L = \frac{J_{sc} A \times G}{1000} \tag{4.16}$$

where, J_{sc} is the short circuit current density (mA/cm^2), A is the area of the PV cell (cm^2), and G is the irradiance (W/m^2). By changing the value of G we got several curves as shown in fig. 2.6(a). It is evident from the curves that the short circuit current reduces significantly with reduced G. The fill factor (eq.4) also reduces to a great extent. Figure 4.6(b) shows the simulated power curves of the PV cell with varying irradiance. Power also reduces proportionally with irradiance.

4.4.2 Effects of the series resistance, R_s:

From fig. 2.7 it can be seen that with the increase of series resistance R_s the open circuit voltage remains the same but both the short circuit current and fill factor reduces

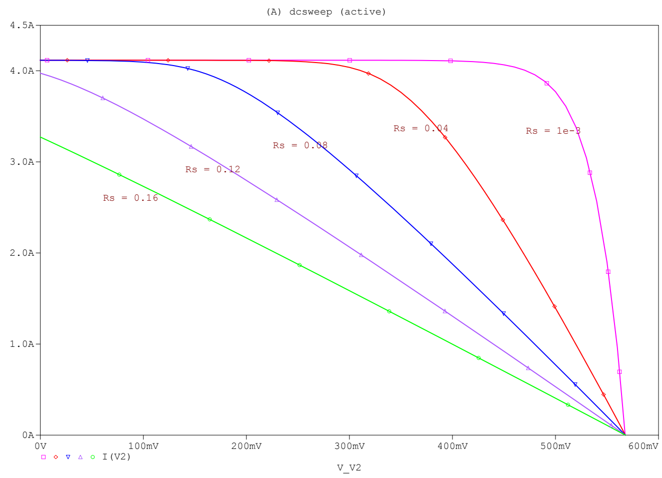

FIGURE 4.7: Effect of series resistance, R_s

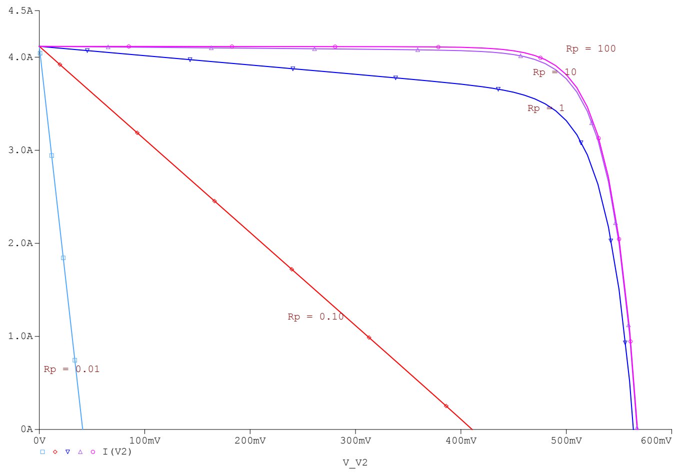

FIGURE 4.8: I-V curves with varying shunt resistance, R_p

significantly. In practice, the value of the lumped series resistance R_s is kept quite low to prevent this drastic degradation in performance.

4.4.3 Effects of the shunt resistance, R_p:

By doing a dcsweep using PSPICE the effect of the shunt resistance ran be found. Figure 4.8 shows the I-V curves with varying shunt resistance R_s. From the figure it can be seen that the value of open circuit current remains same but short circuit current and fill factor reduces with increase in shunt resistance.

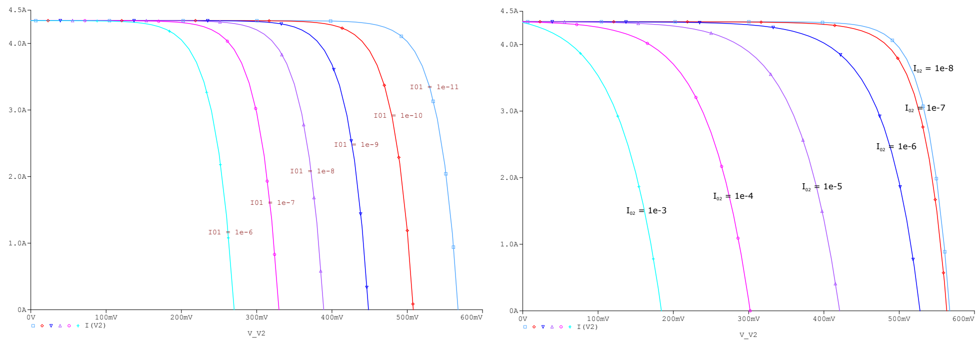

(a) I-V curves with varying dark current, I_{01} (b) I-V curves with varying dark current, I_{02}

FIGURE 4.9: Effects of diffusion diode: (a) I-V curves with varying dark current, I_{01}, and effects of recombination diode: (b) I-V curves with varying dark current, I_{02}

4.4.4 Effects of the diffusion and recombination diode, D_1 and D_2:

Usually the diffusion diode, D_1 has an ideality factor close to unity. But in practice because of the fabrication process some non-ideality may remain. Similarly, the recombination diode should have the ideality factor as 2. But it also exhibits some extents of non-ideality because of the manufacturing process. The impact of both D_1 and D_2 is shown in fig. 2.9 (a) and (b). It is evident that in both cases the short circuit current remains same but the open circuit voltage and fill factor reduces to great extent.

4.4.5 Temperature effects, T_{cell}:

Because of the semi-conductive property of the solar cell, temperature has a strong effect on its performance. In practice solar cell can easily be warmed up to 60-65°C. Using the built in feature temperature sweep of PSPICE we can check the effect of temperature on solar cell operation. Figure 4.10 shows the effect of cell temperature on its performance. It is seen that increased cell temperature reduces the open circuit voltage and fill factor and thus reduces its performance significantly.

4.4.6 Experimental Results

The experimental I-V curves provided by the manufacturer at different illumination and ambient temperature are shown in fig. 2.11 (a). The measured I-V curve at 45 °C and approximately 800 W/m^2 is shown at fig. 2.11 (b). From the figures it is clear that with increase of insolation short circuit current increases drastically but open circuit voltage

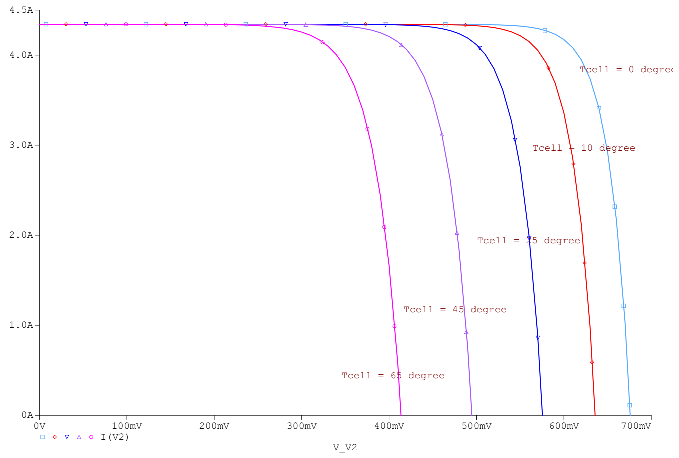

FIGURE 4.10: Effect of operating temperature variation on the performance of PV cell

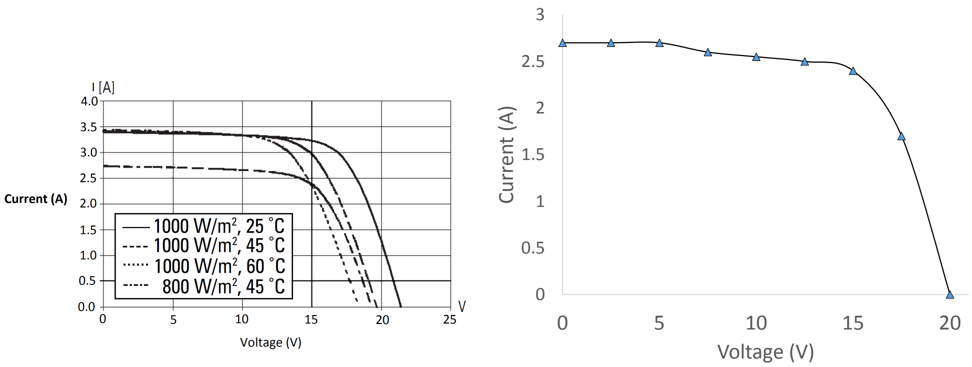

(a) (b)

FIGURE 4.11: Experimental I-V curves (a) provided by the manufacturer at different illumination and ambient temperature and (b) measured at 45 °C and approximately 800 W/m^2

does not increase that much. With the increase of temperature short circuit current does not decrease but open circuit voltage decreases a lot. The experimental results matches with the simulation perfectly.

4.5 Conclusion

The development of PV system raised the need of simulation of PV system. In this paper, all the modeling methods have been discussed and SPICE simulation is done to evaluate the impact of model parameters on the operation of PV cell. The models discussed here are ideal single diode model, single diode R_s model, single diode R_p model, the two diode model, and the three diode model. All the model parameters are enlisted in Table 4.2. The effect of the parameters are discussed with PSPICE simulation. The photocurrent,

I_L is proportional to irradiance, and the series resistance, R_s reduces the short circuit current and fill factor. The parallel resistance, R_p reduces the open circuit voltage, and both the diffusion diode and recombination diode reduces the open circuit voltage value. Finally, increase in cell operating temperature reduces the open circuit voltage and fill factor and thus degrade the performance significantly.

Chapter 5

Optimization of Amorphous Silicon p-i-n Cell

The performance of a solar photovoltaic cell depends on its design, material properties, and fabrication technology [1]. Numerical simulation is the best approach for optimization of a solar cell, which helps to find out the best structure with good fitted parameters. As a result, fabrication complexity, costs, and time reduce significantly. The major objectives of numerical modeling and simulation in solar cell research are testing the validity of proposed physical structures, geometry on cell performance, and fitting of modeling output to experimental results [6]. The numerical modeling has become indispensable tools for designing a high-eïňČciency solar cell [75–77]. Numerical modeling is increasingly being used to obtain insight into the details of the physical operation of thin-film solar cells [78, 79]. Over the years, several modeling tools specific to thin-film PV devices such as AFORS-HET, AMPS-1D, and SCAPS-1D have been developed [80–83]. These tools have already been reached in a mature status and are available to the PV community.

Typically, amorphous silicon thin film solar cells use a p-i-n structure. Because of the "built in" electric field of the p-i-n structure, the bands are tilted, and with electrons donated from the n-layer to the p-layer a built in potential is established [84]. Many researchers have studied this p-i-n structure for various applications [85–87]. Improvement of performance of p-i-n cell is still a subject of research [88–91].

The objective of this study was to design and analyze the thin film single junction hydrogenated amorphous silicon (aSi:H) p-i-n device and optimize its performance by tuning of its various parameters. The research has been carried out with AFORS-HET modeling and computer simulation program. Each of the simulations of the current-voltage (J-V) characteristics and external quantum efficiencies in this paper were done at a device temperature $T = 300K$.

5.1 Methodology

AFORS-HET can simulate one dimensional semiconductor structures by numerical methods with appropriate boundary conditions under steady-state conditions and under small sinusoidal perturbations [92]. To do this, the coupled partial differential equations set is transformed into non-linear algebraic equations set by finite difference methods. At bulk condition, the following one dimensional Poisson's equation and the transport equation for electrons and holes are solved:

$$\frac{\varepsilon_0 \varepsilon_r}{q} \frac{\partial^2 \phi(x,t)}{\partial x^2} = p(x,t) - n(x,t) + N_D - N_A + \sum_{defects} \rho_t(x,t) \tag{5.1}$$

$$-\frac{1}{q} \frac{\partial j_n(x,t)}{\partial x} = G_n(x,t) - R_n(x,t) - \frac{\partial}{\partial t} n(x,t) \tag{5.2}$$

$$\frac{1}{q} \frac{\partial j_p(x,t)}{\partial x} = G_p(x,t) - R_p(x,t) - \frac{\partial}{\partial t} p(x,t) \tag{5.3}$$

where, n is the electron density, p is the hole density, and ϕ is the electric potential for which the system of differential equations is solved. q is the electron charge, ε_0, ε_r are the absolute and relative dielectric constants respectively, N_D, and N_A are the concentrations of donors and acceptors respectively. The distribution function f_t describes the charge stored in the defects, specifying the probability that defects with defect density N_t at the position E within the bandgap are occupied with electrons:

acceptor-type defect:

$$\rho_t(x,t) = -\int dE f_t(E,x,t) N_t(E) \tag{5.4a}$$

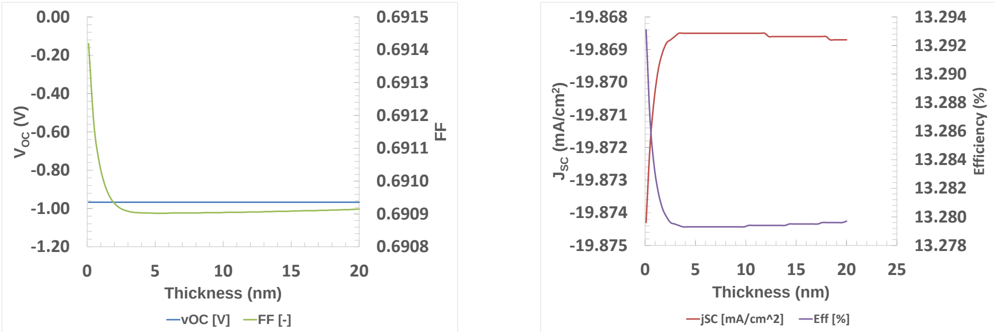

(a) (b)

FIGURE 5.1: Effect of n-layer thickness variation on (a) V_{OC} and FF (b) J_{SC} and Efficiency

donor-type defect:

$$\rho_t(x,t) = \int dE(1 - f_t(E,x,t))N_t(E) \tag{5.4b}$$

The rest of the detailed derivation is skipped here which can be found at [92–95]. The details of these equations and implementations are also given in Appendix A.

The efficiency and short circuit current density of the p-i-n cell depend on design parameters like window layer thickness, donor and acceptor concentrations, electron and hole mobility, band-gap, and band-tail states. In fact, all the optical parameters for single crystal material are applicable for amorphous semiconductor [6]. However, the low mobility and large number of localized gap states create the difference in amorphous semiconductor. By adjusting these input parameter values best performance cell structure can be found.

5.2 Results and Discussion

The best performed cell structure is found by using parameters variation tool of AFORS-HET program. Figure 5.1 shows the effect of p-layer thickness variation on open circuit voltage (V_{OC}), Fill Factor (FF), short circuit current density (J_{SC}), and Efficiency (E_{FF}). From this figure, it can be seen that V_{OC} decreases with increase of thickness and FF also decreases with thickness of p-layer. On the other hand, J_{SC} decreases with increase of

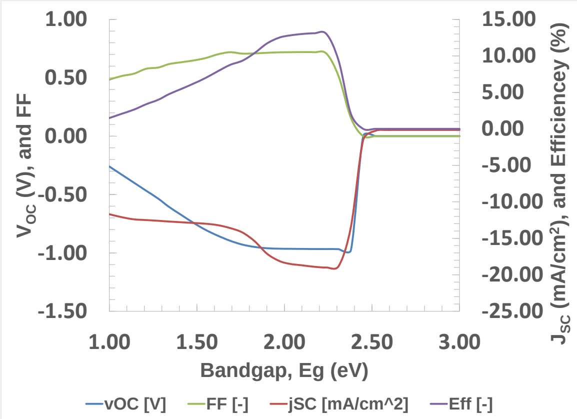

FIGURE 5.2: Impact of window (p)-layer bandgap on V_{OC}, J_{SC}, FF and Efficiency

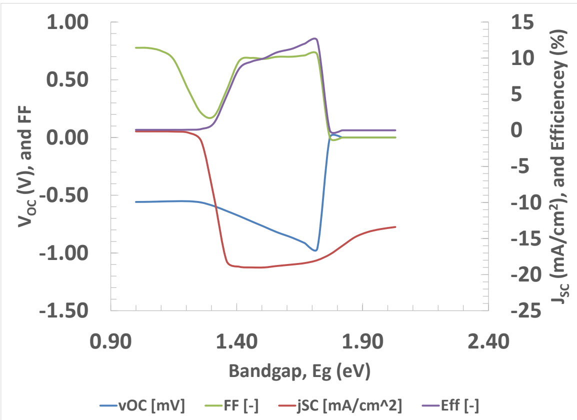

FIGURE 5.3: Effect of i-layer bandgap variation on V_{OC}, J_{SC}, FF and Efficiency

TABLE 5.1: Input values of parameters of the best performed p-i-n cell

Parameters	p- aSi:H	i- aSi:H	n-aSi:H
Layer thickness, L(nm)	1.12	1600	1.02
Relative permittivity	11.9	11.9	11.9
Electron mobility,	20	20	20
Hole mobility	5	5	5
Na(cm-3)	1.01E+21	0	0
Nd (cm-3)	0	0	1.00E+20
Eg (eV)	2.17	1.72	2.08
Nc (cm-3)	1.00E+20	1.00E+20	1.00E+20
Nv (cm-3)	1.00E+20	1.00E+20	1.00E+20
Electron affinity,	3.9	3.9	3.9

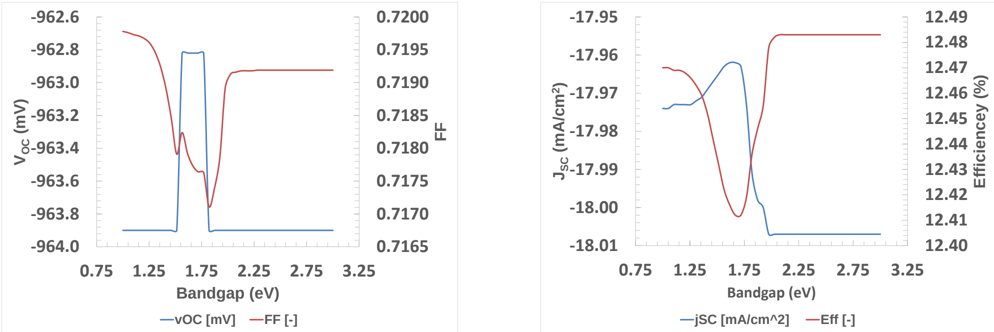

(a) (b)

FIGURE 5.4: Effect of n-layer bandgap variation on (a) V_{OC} and FF (b) J_{SC} and Efficiency

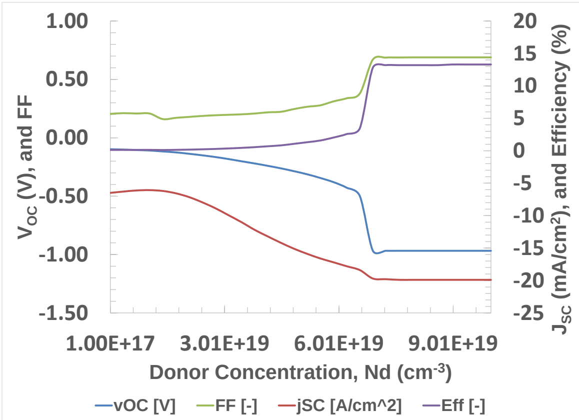

FIGURE 5.5: Impact of n-layer doping concentration on V_{OC}, J_{SC}, FF and Efficiency

the p-layer thickness and maximum efficiency is achieved with p-layer thickness between 0.5-2 nm.

Figure 5.2 shows similar kind of graph with result of i-layer thickness variation on the V_{OC}, J_{SC}, FF and Efficiency. It is evident that J_{SC} increases with increase of i-layer width but V_{OC} decreases with increase of width. However, increasing thickness beyond 500 nm has no significant change either in V_{OC}, or J_{SC} and thus efficiency remains approximately constant.

Figure 5.3 shows that, the optimum n-layer thickness is between 0.5-1 nm. Beyond this range J_{SC}, FF and Efficiency all decreases. However, V_{OC} remains approximately same for n-layer width variations.

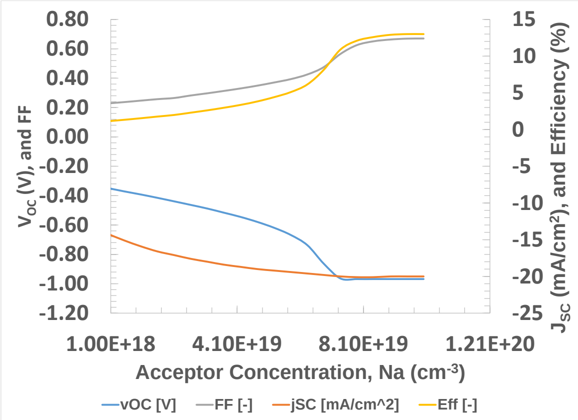

FIGURE 5.6: Effect of p-layer doping concentration variation on V_{OC}, J_{SC}, FF and Efficiency

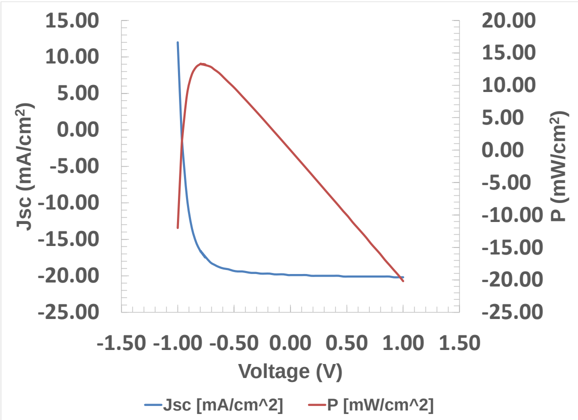

FIGURE 5.7: J-V and P-V curve of the best performed p-i-n cell under AM 1.5 and 1000 W/m^2

The impact of window layer bandgap on V_{OC}, J_{SC}, FF and Efficiency is illustrated in Figure 5.4. It is seen from the graph that optimum window layer bandgap is achieved within bandgap of 1.9-2.2 eV. Lowering the bandgap below 1.9 eV reduces all the I-V characteristics parameters and efficiency is also decreased.

Figure 5.5 illustrates the effect of i-layer bandgap variations on V_{OC}, J_{SC}, FF and Efficiency. The optimal bandgap lies in between the range of 1.65-1.75 eV.

Figure 5.6 shows the effect of n-layer bandgap variation and it is found that maximum efficiency is achievable withing the bandgap of 1.95-2.05 eV.

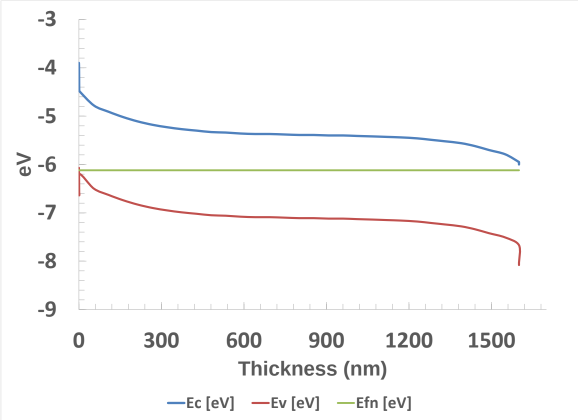

FIGURE 5.8: Band diagram of the optimum p-i-n cell under equilibrium condition

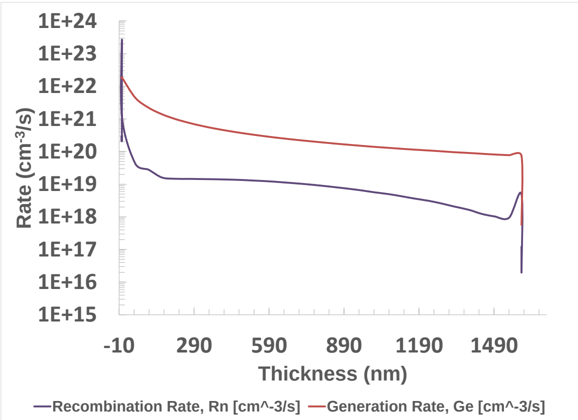

FIGURE 5.9: Generation and recombination rate of be best performed p-i-n cell

The impact of doping concentrations of p and n- layer are shown in Figure 5.7 and 4.8. Optimal value for donor concentration for n-layer is found to be above $7 \times 10^{19} cm^{-3}$ and acceptor concentration for p-layer is found to be above $8.1 \times 10^{19} cm^{-3}$.

Finally, taking these optimal cell parameters the best performed single junction p-i-n cell is designed and simulated. Table 5.1 shows the input parameters of the best performed p-i-n cell.

Figure 5.9 shows the illuminated J-V and P-V curve of the best performed p-i-n cell. The calculated light J-V characteristics of the cell yield the following results:

Short circuit current density of $J_{SC} = -19.87 mA/cm^2$,

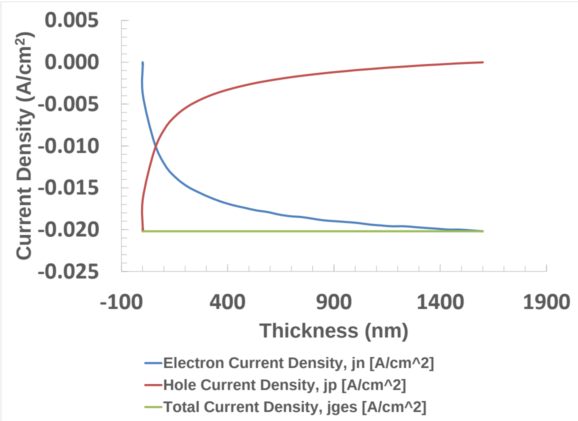

FIGURE 5.10: Current density of the p-i-n cell

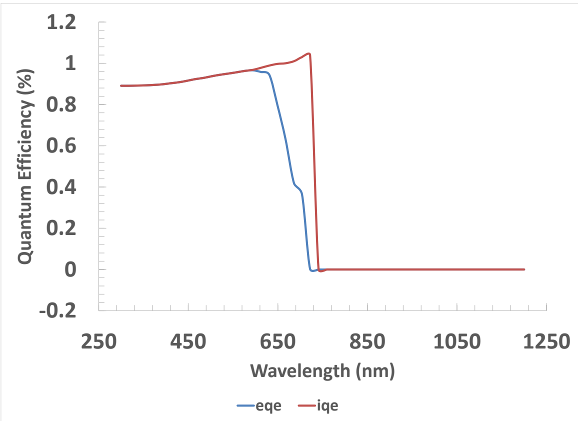

FIGURE 5.11: Internal and external quantum efficiency of the p-i-n cell

Open circuit voltage $V_{OC} = -0.967V$,

Fill-factor $FF = 0.689$,

Efficiency = 13.26 %.

The band diagrams under equilibrium condition are shown in Figure 5.10. The bands are tilted as expected from aSi:H p-i-n cell. The fermi level is at 6.1 eV.

Figure 5.11 shows the generation and recombination rate of charge carriers in the cell. It can be seen that the front and back surface has a higher recombination rate than in between. Surface passivation layer would improve the cell's overall performance in this situation.

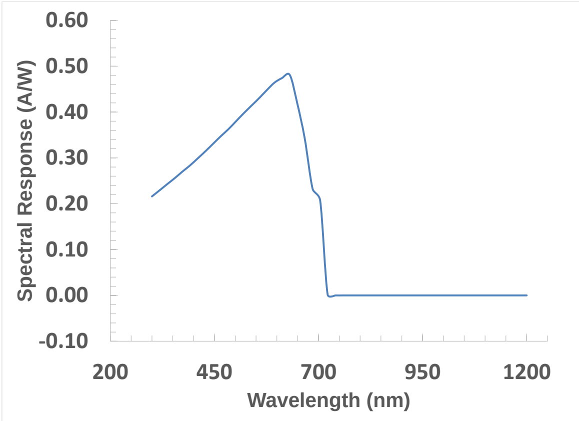

FIGURE 5.12: Spectral response of the optimal p-i-n cell

Figure 5.12 shows the current densities of the p-i-n cell. The total output current density remained around $-20mA/cm^2$ which is quite good for a p-i-n cell.

The internal and external quantum efficiencies and spectral response under AM 1.5 are shown in figure 5.13 and 5.14 respectively. It is evident from these graph that due to higher band-gap of aSi:H silicon, the above mentioned p-i-n cell has spectral response only below wavelength of 700 nm. With respect to a band gap of around 2 eV, the band gap utilization is relatively low due to the high levels of Shockley-Red-Hall (SRH) recombination and the relative broad valence and conduction-band tails.

5.3 Conclusion

With AFORS-HET simulation software, the best efficiency of this numerically designed single junction aSi:H solar cell is 13.26% with intrinsic layer thickness of 1600 nm and optimum window layer bandgap of 2.17 eV. The obtained results show that the surface recombination speeds of front and back contact is crucial to short circuit current density and efficiency of aSi:H solar cell. Therefore one can increase the performance of aSi:H solar cell by minimizing the surface recombination speed of the front and back surface as well as the interface of transparent conducting oxide. The Quantum Efficiency (QE) curve shows that the cell has good spectral response in the wavelength range $400nm$ – $650nm$ which means that it would be a good candidate as a top cell of double junction or micromorph solar cell configuration and as a middle cell in triple junction structure.

Chapter 6

Optimization of Microcrystalline Silicon p-i-n Cell

Although microcrystalline silicon has superior properties than amorphous material, the μc-Si:H p-i-n cell showed $\approx$2-3% lower efficiency than amorphous p-i-n cell [96]. However, the tandem structure with a-Si:H as top cell and μc-Si:H as bottom cell, which is called the micromorph cell, showed better stability with higher efficiency of 14.5% [97, 98]. The micromorph structure needs at least 6 layers and for better performance back surface field (BSF layer) and intermediate reflectors (e.g. ZnO layer) are added which increases the number of layer up to 8 [14]. This large number of layers increases the complexity of fabrication process along with rise in cost. Besides these, because of interfacial mismatch and defects, production of high quality solar cell is quite difficult. Hence, single junction p-i-n cell is more suitable for easy fabrication. Since, μc-Si:H has a simple deposition process and it is less prone to Staebler-Wronski Effect (SWE), there is good research scope for this material. Optimizing the structural parameters of the p-i-n cell would be the first step toward the improvement of efficiency.

The objective of the study on this chapter was to design and analyze the thin film single junction hydrogenated microcrystalline silicon (μc-Si:H) p-i-n device and optimize its performance by tuning of its various parameters. The research has been carried out with AFORS-HET modeling and computer simulation program.

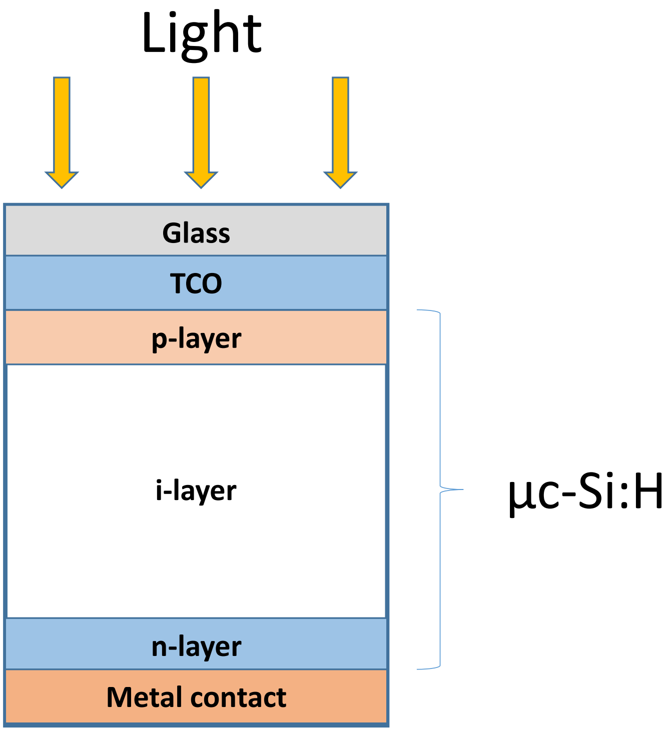

FIGURE 6.1: Schematic diagram of μc-Si:H p-i-n cell

6.1 Methodology

6.1.1 Simulation Details

Each of the simulations of the current-voltage (J-V) characteristics and external quantum efficiencies in this paper were done at a device temperature $T = 300K$. AM 1.5 spectrum with 100 mW/cm^2 illumination source is used to find the illuminated cell conditions. Light is illuminated from the front side of the cell as shown in Figure 6.1. Glass is used as the substrate followed by a thin transparent conducting oxide (TCO), a thin p-layer, an i-layer, and n-layer with metal contacts at the back side. Indian tin oxide (ITO) or ZnO can be used as TCO and Ag or Al can be used as the back contact.

In μc-Si:H material there are disordered regions and voids as in the case of amorphous material, except it has mixture of crystalline grains ranging from few nanometers to more than a micrometer size [14]. Because of these crystal grains microcrystalline silicon has better carrier transport than amorphous material [7]. To model this microcrystalline structure two Gaussian type defects- one for acceptors and the other for donators were introduced in the bulk layers. Two tail states- one for valence band and one for conduction

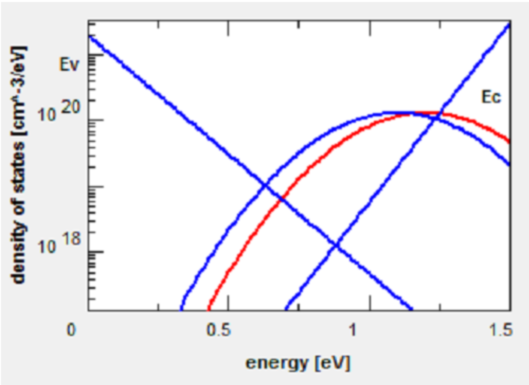

(a) p-layer

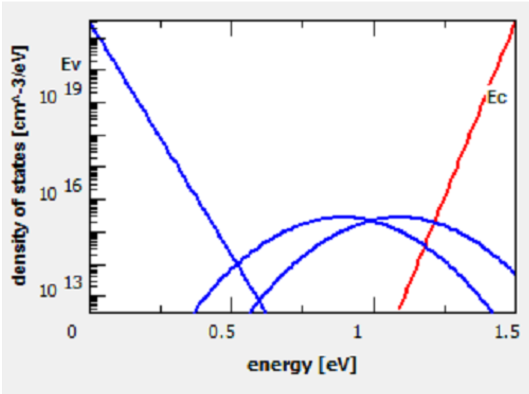

(b) i-layer

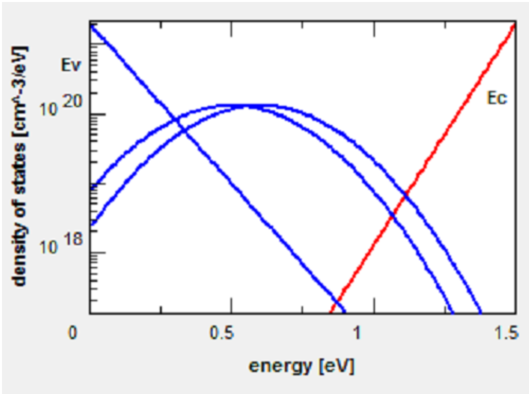

(c) n-layer

FIGURE 6.2: Defect state distributions of μc-Si:H layers of p-i-n cell in the simulations

band are also defined for each layer. The defect state distributions of μc-Si:H layers of p-i-n cell in the simulations are shown in Figure 6.2.

Input parameters of the baseline μc-Si:H p-i-n structure used in the simulations are given in Table 6.1. Unless otherwise stated in Table 6.1, all the default values of AFORS-HET were adopted. It is here to be noted that the basic parameters shown in Table 6.1 are taken from standard references [15, 99].

According to density of state model, both amorphous and microcrystalline silicon contain acceptor-like states above the mid gap and donor-like states below the mid gap. This is because of the dangling bonds or defects introduced at the outer part of the crystal lattice and grain boundaries [14]. However, microcrystalline silicon shows somehow lower effective conduction band density (N_c) and valence band density (N_v). This is because of the crystalline grains presence in the material. That is why values of N_c and N_v are kept one order lower than that of amorphous silicon. Because of the same reason electron mobility and hole mobility are kept little higher.

TABLE 6.1: Input parameters of the baseline μc-Si:H p-i-n structure used in the simulations

Parameters	**p-layer**	**i-layer**	**n-layer**
Layer thickness, L(nm)	variable	variable	variable
Dielectric constant	11.9	11.9	11.9
Bandgap, Eg (eV)	variable	variable	variable
Electron mobility,	50	50	50
Hole mobility	5	5	5
Acceptor concentration, $N_a(cm^{-3})$	variable	0	0
Donator concentration, $N_d(cm^{-3})$	0	1000	variable
Effective DOS conduction Band, $N_c(cm^{-3})$	10^{19}	10^{19}	10^{19}
Effective DOS valence Band, $N_v(cm^{-3})$	10^{19}	10^{19}	10^{19}
Electron affinity (eV)	3.9	3.9	3.9
Valence Band tail states parameters			
VB trap density (cm-3)	2.40×10^{20}	9.40×10^{19}	1.88×10^{20}
VB tail characteristic energy (meV)	120	30	94
Electron capture cross section (cm^2)	7.00×10^{-16}	7.00×10^{-16}	7.00×10^{-16}
Hole capture cross section (cm^2)	7.00×10^{-16}	7.00×10^{-16}	7.00×10^{-16}
Conduction Band tail states parameters			
CB trap density (cm^{-3})	2.40×10^{20}	6.40×10^{19}	1.36×10^{20}
CB tail characteristic energy (meV)	80.00	20.00	68.00
Electron capture cross section (cm^2)	7.00×10^{-16}	7.00×10^{-16}	7.00×10^{-16}
Hole capture cross section (cm^2)	7.00×10^{-16}	7.00×10^{-16}	7.00×10^{-16}
Gaussian defect states parameters (Acceptor)			
Defect density (cm^{-3})	6.90×10^{19}	1.00×10^{15}	6.90×10^{19}
Standard deviation (Gaussian) (eV)	0.21	0.144	0.21
Electron capture cross section (cm^2)	3.00×10^{-15}	1.00×10^{-15}	3.00×10^{-15}
Hole capture cross section (cm^2)	3.00×10^{-14}	1.00×10^{-14}	3.00×10^{-14}
Gaussian defect states parameters (Donator)			
Defect density (cm^{-3})	6.90×10^{19}	1.00×10^{15}	6.90×10^{19}
Standard deviation (Gaussian) (eV)	0.21	0.144	0.21
Electron capture cross section (cm^2)	3.00×10^{-14}	1.00×10^{-14}	3.00×10^{-14}
Hole capture cross section (cm^2)	3.00×10^{-15}	1.00×10^{-15}	3.00×10^{-14}

The efficiency, short circuit current density, open circuit voltage, and fill factor of the p-i-n cell depend on design parameters like window layer thickness, donor and acceptor concentrations, electron and hole mobility, band-gap, and band-tail states. In fact, all the optical parameters for single crystal material are applicable for microcrystalline material [6]. However, the low mobility and large number of localized gap states create the difference. In this work, the input parameters like layer thickness, bandgap, donor and acceptor concentrations are varied to find best performance cell structure.

6.2 Results and Discussions

6.2.1 Optimization of layer thickness

Layer thickness plays an important role in the optimization of a p-i-n device. As p-layer is actually the window layer, its thickness is varied from 1nm - 100 nm. Because of the indirect bandgap property of μc-Si:H it is essential to have a thick intrinsic layer for better absorption of photons. Therefore, i-layer is varied from several nanometers to 10 micrometers. The n-layer is kept within the 100 nm range and varied to find the optimum thickness for better electron transport.

Figure 6.3 illustrates the effect of thickness variation on J_{SC}, V_{OC}, FF, and Efficiency. From figure 6.3 (a) and 6.3 (b) it is evident that a thin p-layer of 1 to 5 nm would result in a better J_{SC}, and V_{OC}, and thus a higher efficiency. With increase in thickness of p-layer the amount of light reaching the absorber layer reduces and results in lower J_{SC} values. It also becomes difficult for the built in field to separate the electron-hole pair if the thickness of p-layer is high.

On the other hand, from figure 6.3 (c) and 6.3 (d) it can be seen that a thicker absorber layer of 8 to 9 μm should be used to get better performance from the p-i-n device. As an indirect semiconductor the μc-Si:H should have a thicker absorber layer to absorb as much photons as possible. However, increasing the thickness beyond 10 μm does not increase the efficiency anymore and the device reaches its saturation. Although J_{SC} increases with the increase of i-layer thickness V_{OC} does not increase that much rather it remains almost constant.

For n-layer the maximum efficiency can be achieved within 1 to 5 nm range where J_{SC} is maximum as shown in figure 6.3 (e) and 6.3 (f). Although J_{SC} decreases with increase of thickness V_{OC} remains constant throughout the variation. This is because of the lower electron and hole mobility of the μc-Si:H where thicker n-layers reduces the electron transport facility.

6.2.2 Optimization of doping concentration

Variation of efficiency along with J_{SC}, V_{OC}, and FF is depicted in figure 5.4 for the variation in acceptor and donor concentration. From figure 6.4 (a) it can be seen that

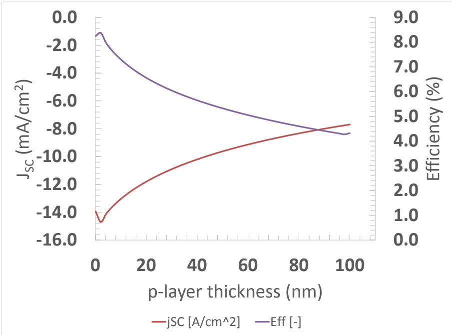

(a) p-layer

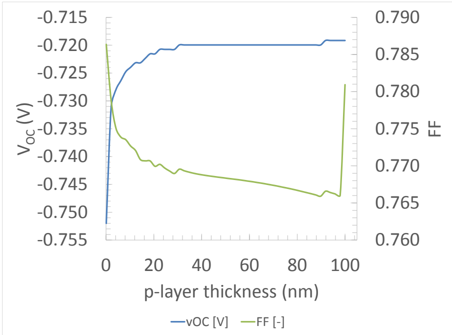

(b) p-layer

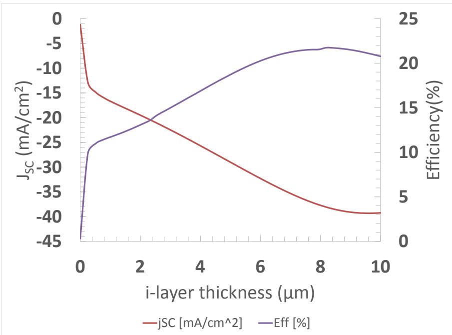

(c) i-layer

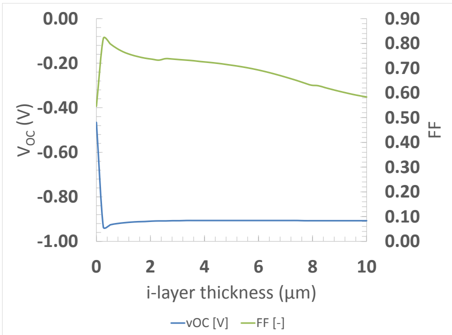

(d) i-layer

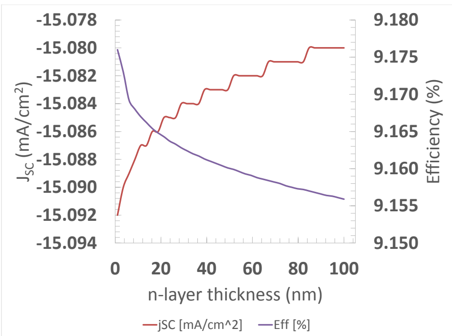

(e) n-layer

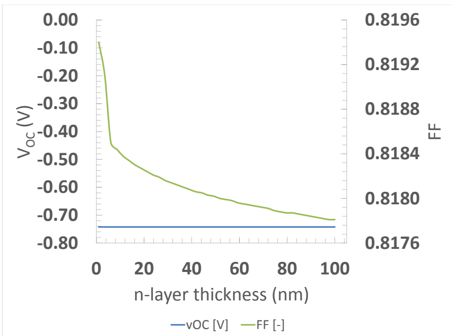

(f) n-layer

FIGURE 6.3: Effect of thickness variation on J_{SC} and efficiency are shown in (a), (c), and (e) for p-, i-, and n-layer respectively. Variation in V_{OC} and FF are shown in (b), (d), and (f) for p-, i-, and n-layer respectively.

efficiency and J_{SC} both increases with increase in acceptor concentration, N_a. However, beyond the acceptor concentration of $10^{19} cm^{-3}$ the efficiency and J_{SC} reaches the maximum value and do not increase further. This is because of the fully crowded states in

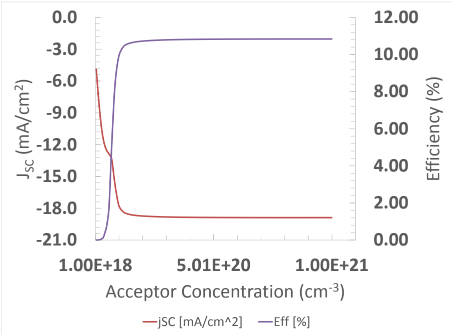

(a) Effect of N_a variation on J_{SC} and Efficiency

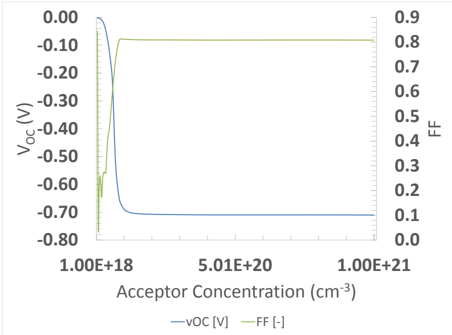

(b) Effect of N_a variation on V_{OC} and FF

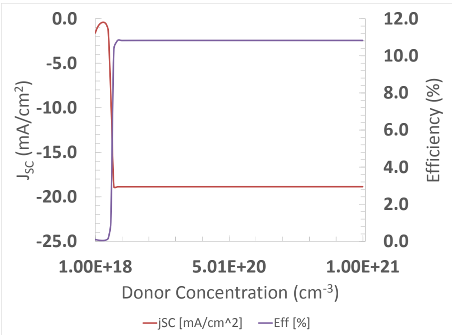

(c) Effect of N_d variation on J_{SC} and Efficiency

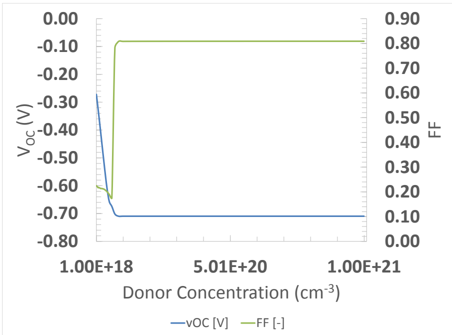

(d) Effect of N_d variation on V_{OC} and FF

FIGURE 6.4: Impact of Acceptor concentration (N_a) and Doping concentration (N_d) variation on J_{SC}, V_{OC}, Efficiency and FF.

the cell which saturates the performance.

It is also seen from figure 6.4 (b) that V_{OC} and FF also reaches to saturation after the $10^{19} cm^{-3}$ limit. In the case of donor concentration, N_d from figure 6.4 (c) and 4 (d) similar kind of trend is also visible. Increasing the donor concentration above $10^{19} cm^{-3}$ does not increase the efficiency further. J_{SC}, V_{OC}, and FF also reaches at maximum value at this limit.

6.2.3 Optimization of Bandgap

Bandgaps of the p-, i-, and n-layer is varied to find the optimum bandgap for the p-i-n device. As for μc-Si:H the bandgap can be obtained from 1.2 eV to 1.5 eV [100], the bandgaps of p-, i-, and n-layer was varied in the specified range for optimization. Effect of bandgap variation on J_{SC} and efficiency are shown in (a), (c), and (e) for p-, i-, and n-layer respectively. Variation in V_{OC} and FF are shown in (b), (d), and (f) for p-, i-, and n-layer respectively. It can be seen from figure 6.5 (a) that J_{SC} reaches to its maximum value with a higher bandgap of the window layer close to 1.5 eV. This is because with increase in p-layer bandgap more photons can reach the absorber layer to produce more current. From figure 6.5 (b) it can be seen that the V_{OC} also follows the similar trend. The reason why V_{OC} also increases can be the lower rate of recombination with higher badgap of window layer.

For i-layer bandgap variation from 1.2 eV to 1.5 eV it can be seen from figure 6.5 (c) and (d) that J_{SC} increases abruptly with increase in i-layer bandgap from 1.2 eV to 1.4 eV. However, it starts to decrease after 1.4 eV. On the other hand, V_{OC} has an approximately linear increasing trend with increase in bandgap. This might be because of the lowering of band offset with increase in bandgap of i-layer. As bandgap of p-layer is kept at 1.5 eV, the low bandgap of i-layer would create a band offset which will eventually increase the recombination. Therefore maximum efficiency is achieved within the 1.4 to 1.5 eV range.

From figure 6.5 (e) it can be seen that J_{SC} does not increase significantly with increase of bandgap from 1.2 to 1.3 eV but it increases abruptly after 1.3 eV and reaches saturation at around 1.45 eV. V_{OC} also shows a similar trend as depicted in figure 6.5 (f). As both p- and i-layer bandgap was kept closer to 1.5 eV the n-layer badgap should also be closer to that value to reduce the recombination losses and increase the V_{OC}.

6.2.4 Design optimized solar cell performance

By taking all the optimal values of the layer thicknesses, bandgap, and doping concentrations and running the simulation using AFORS-HET the characteristics of the best performed cell was found. Table 6.2 shows the optimum parameters found in the simulation and used to design the best-performed c-Si:H p-i-n cell.

Illumination of 1000 W/m^2 at AM 1.5 was used to find the J-V and P-V curves shown in figure 6.6. The calculated light J-V characteristics of the cell yield the following results:

Short circuit current density of J_{SC} = -33 mA/cm^2,

Open circuit voltage VOC = -906.5 mV ,

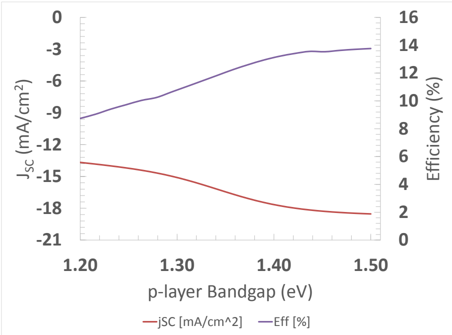

(a) p-layer

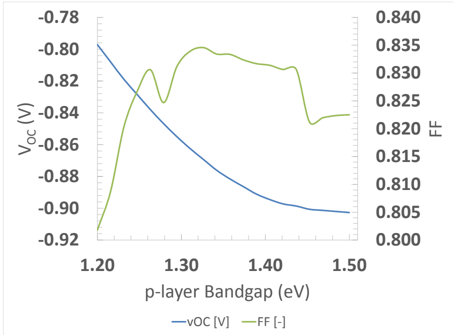

(b) p-layer

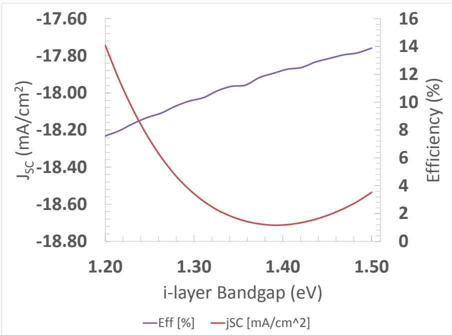

(c) i-layer

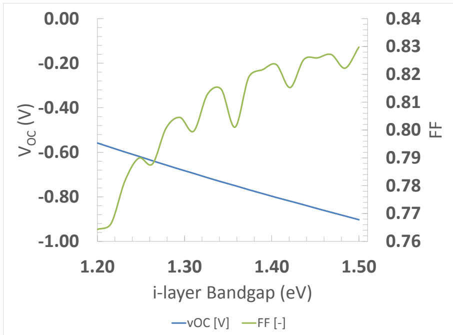

(d) i-layer

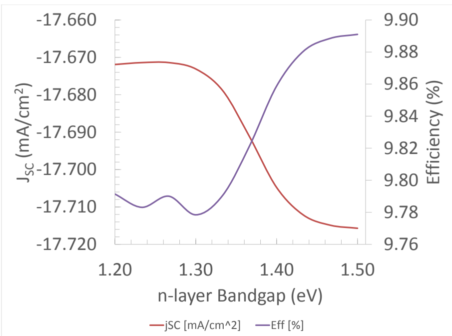

(e) n-layer

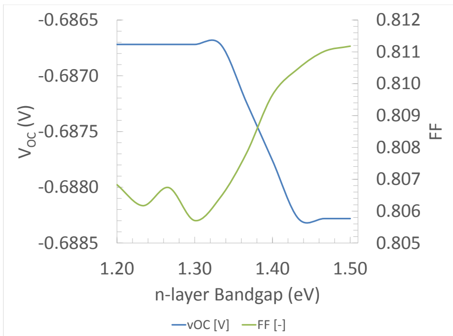

(f) n-layer

FIGURE 6.5: Effect of bandgap variation on J_{SC} and efficiency are shown in (a), (c), and (e) for p-, i-, and n-layer respectively. Variation in V_{OC} and FF are shown in (b), (d), and (f) for p-, i-, and n-layer respectively.

Fill-factor FF = 0.694,

Efficiency = 20.78 %.

TABLE 6.2: Optimum parameters found in the simulation and used to design the best-performed cell

Parameters	p- cSi:H	i- cSi:H	n-cSi:H
Layer thickness, L(nm)	1	6000	20
Na(cm-3)	5.00E+20	0	0
Nd (cm-3)	0	1000	1.00E+20
Eg (eV)	1.5	1.5	1.5

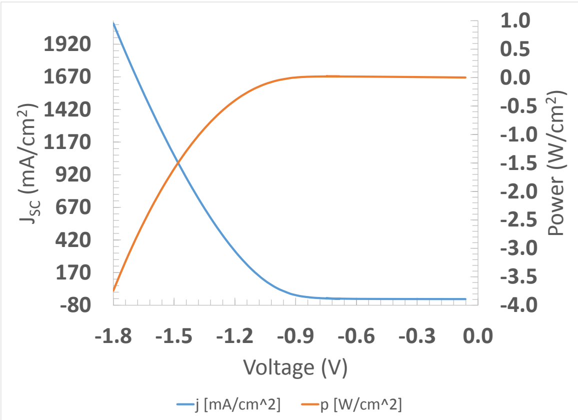

FIGURE 6.6: J-V and P-V curve of the best performed μc-Si:H p-i-n cell under AM 1.5 and 1000 W/m^2 illumination

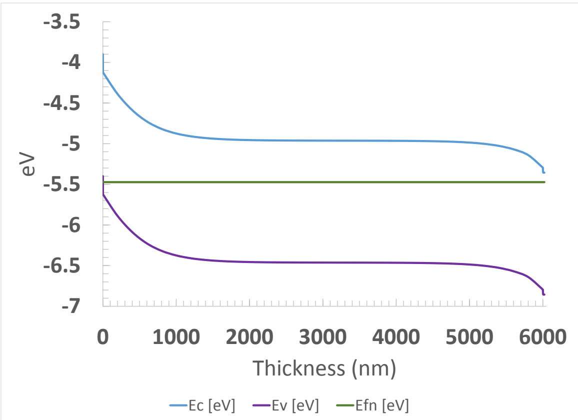

FIGURE 6.7: Band diagram of the optimum cell under equilibrium condition

Figure 6.7 shows the band diagram of the optimum cell under equilibrium condition. The fermi level was found at -5.47 eV. The generation and recombination rate of the designed cell is illustrated in figure 6.8. It can be seen that the recombination rate is much higher at the front and back surface of the cell. This can be reduced by adding

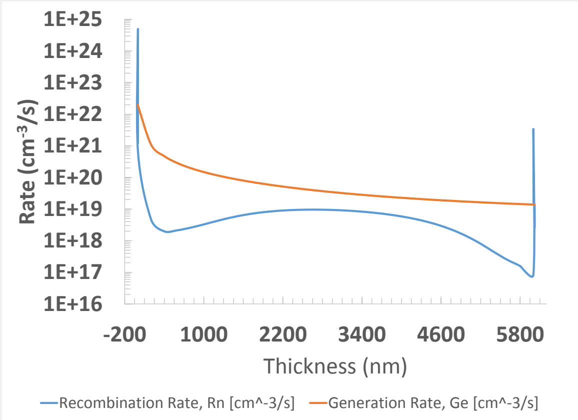

FIGURE 6.8: Generation and recombination rate of be best performed cell

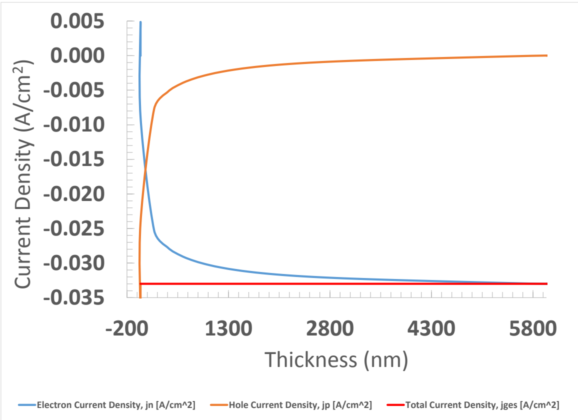

FIGURE 6.9: Current density of the p-i-n cell

surface passivation layers.

Figure 6.9 shows the electron and hole current densities with the variation of thickness of the device. The total output current density remained at around -33 mA/m^2 which is pretty high for a bare p-i-n cell. This indicates that a well-designed c-Si:H p-i-n cell can have a higher current density and better performance.

Figure 6.10 illustrates the internal and external quantum efficiencies of the cell. The external quantum efficiency reached a maximum of 96.42 % at wavelength (λ) of 678 nm. The overall external quantum efficiency remained very high from 87-96 % for wavelength of 550-650 nm range. This indicates that the cell will perform its best under visible light wavelengths. Figure 6.11 shows the spectral response of the cell which also indicates

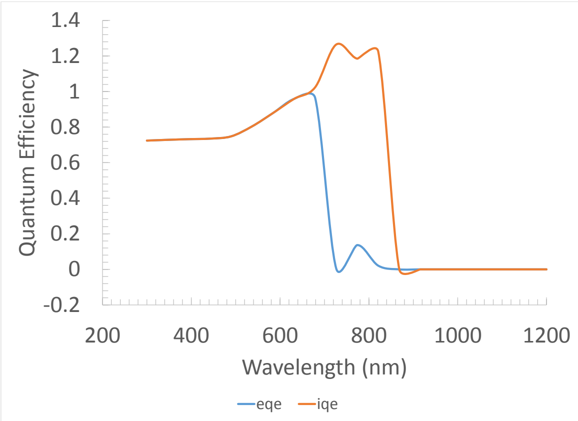

FIGURE 6.10: Internal and external quantum efficiency of the p-i-n cell

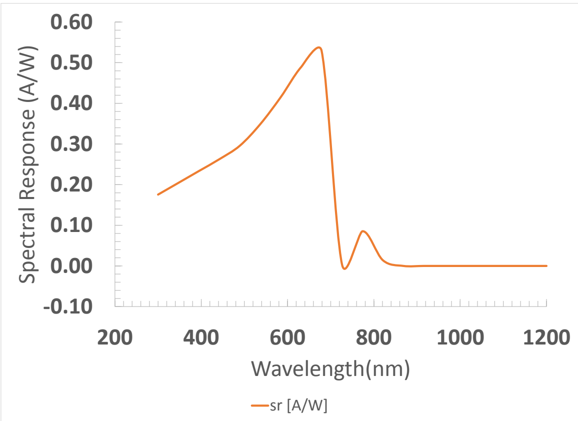

FIGURE 6.11: Spectral response of the optimal p-i-n cell

the similar scenario. It can easily be decided that the designed p-i-n can be used as the bottom cell of a micromorph tandem cell.

6.3 Conclusion

With AFORS-HET simulation software, the parameters like bandgap, layer thickness, and doping concentrations of a c-Si:H p-i-n cell are varied. From the simulation it is found that the p-layer thickness should be as small as possible close to 1 nm whereas the i-layer of the cell should have a thickness in the range of 5-8 μm. The n-layer thickness should also be in between 10-20 nm range for better performance. The doping concentrations are also varied and maximum efficiency of around 20 % is achieved with acceptor concentration of $5 \times 10^{20} cm^{-3}$ and donor concentration of $1 \times 10^{20} cm^{-3}$. The bandgap of p-, i-, and n-layer are also varied and optimum performance is found at higher bandgaps closer to 1.5 eV.

Finally, using these values an optimum cell is numerically designed and simulated. It is found that the best-performed cell has a short circuit current density of -33 mA/cm^2, open circuit voltage of -906.5 mV, fill factor of 0.694, and efficiency of 20.78%. The cell has higher front and back surface recombination speeds which can be reduced by surface passivation. The quantum efficiency and spectral response curves also showed that the cell has a very good spectral response in the 550-650 nm range which makes it a good candidate for a bottom cell of a micromorph or double junction cell and a middle cell for a triple junction cell.

Chapter 7

Optimization of Micromorph Tandem Cell

Meier et al. [101] first introduced the micromorph concept for high efficiency achievement. Later on, various researches have been done on various aspects like- light trapping [102–104], deposition process [105–107], use of intermediate reflector [19, 108–112], optimization of absorber layer thickness [113], and front surface texturing [114] of micromorph cell. However, the efficiency, short circuit current density, open circuit voltage, and fill factor of the micromorph device depends on design parameters like layer thicknesses of different layers, donor and acceptor concentrations, band-gap, and band-tail states. In fact, the low mobility and large number of localized gap states of both amorphous and microcrystalline material reduces the output significantly.

In this work, the device parameters like- layer thickness, bandgap, donor and acceptor concentrations are varied to find optimum structure of micromorph tandem solar cell. Besides this, the performance of that optimal device is also simulated using numerical simulation software AFORS-HET.

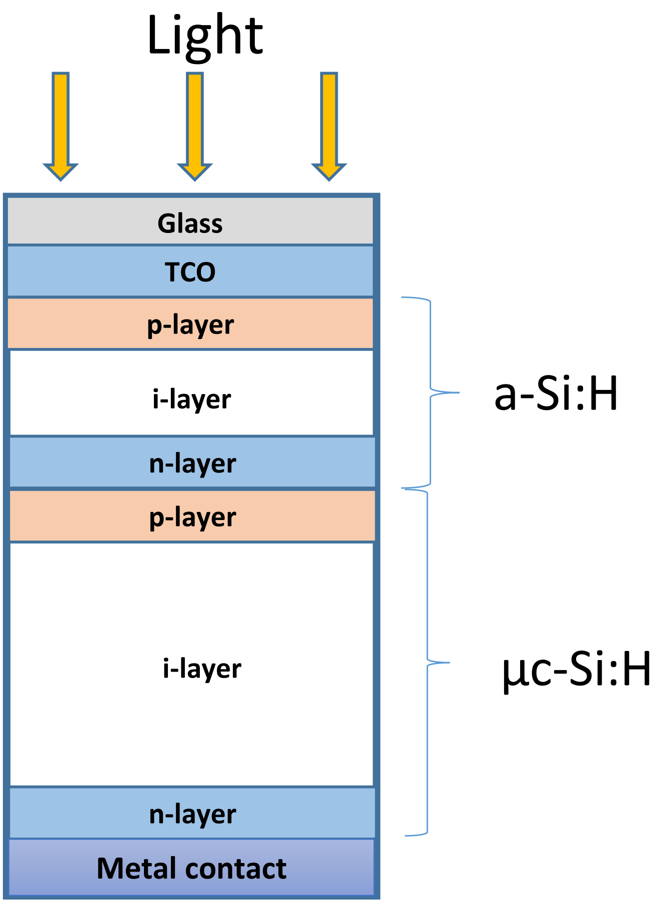

FIGURE 7.1: Schematic diagram of a-Si:H top cell and μc-Si:H bottom cell micromorph tandem device

7.1 Methodology

7.1.1 Simulation Details

Each of the simulations of the current-voltage (J-V) characteristics and external quantum efficiencies in this paper were done at a device temperature $T = 300K$. AM 1.5 spectrum with 100 mW/cm^2 illumination source is used to find the illuminated cell conditions. Light is illuminated from the front side of the cell as shown in Figure 7.1. Glass is used as the substrate followed by a thin transparent conducting oxide (TCO), a thin a-Si:H p-, i-, and n-layer followed by μc-Si:H p-, i-, and n-layer with metal contacts at the back side. Indian tin oxide (ITO) or ZnO can be used as TCO and Ag or Al can be used as the back contact.

In both a-Si:H and μc-Si:H material there are disordered regions and voids, except μc-Si:H material which has mixture of crystalline grains ranging from few nanometers to more

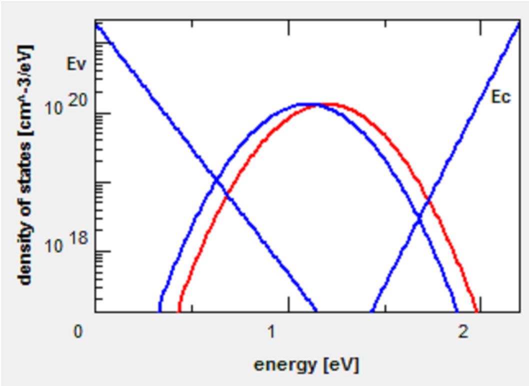

(a) a-Si:H p-layer

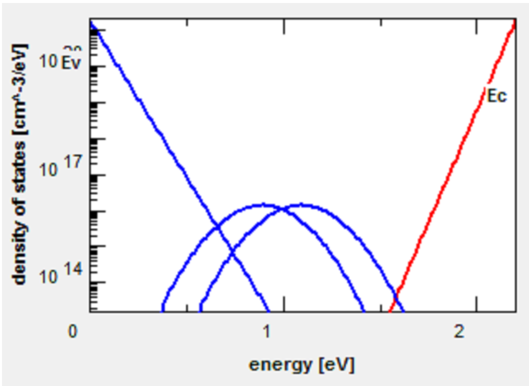

(b) a-Si:H i-layer

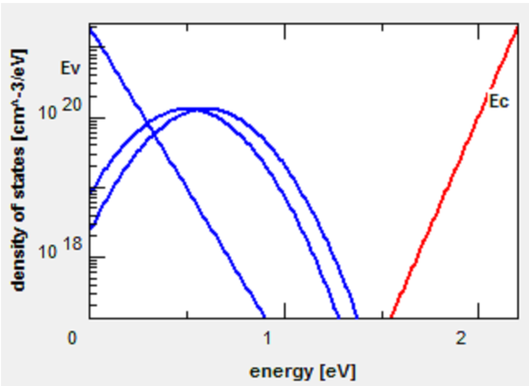

(c) a-Si:H n-layer

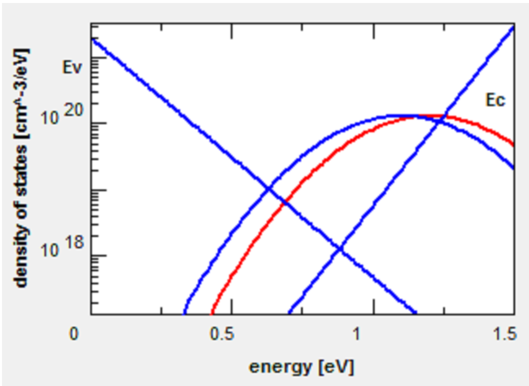

(d) μc-Si:H p-layer

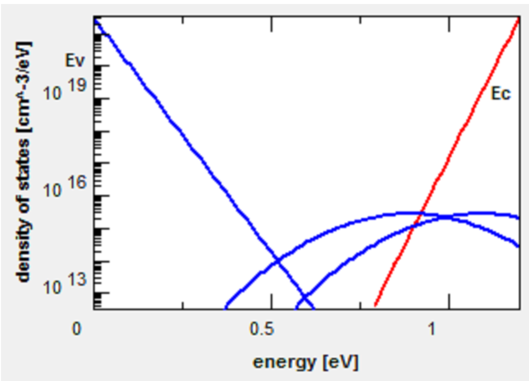

(e) μc-Si:H i-layer

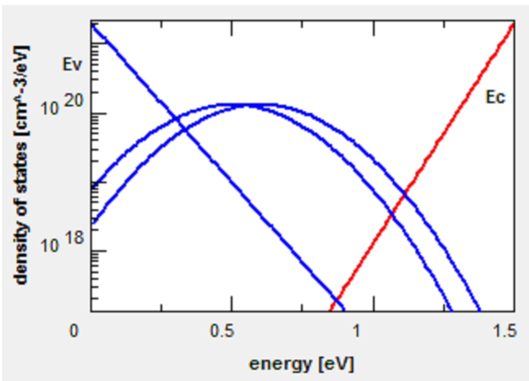

(f) μc-Si:H n-layer

FIGURE 7.2: Defect state distributions of a-Si:H and μc-Si:H layers of micromorph cell in the simulations

than a micrometer size [14]. To model these amorphous and microcrystalline structures two Gaussian type defects- one for acceptors and the other for donators were introduced in the bulk layers along with two tail states- one for valence band and one for conduction band for both materials are also defined for each layer. The defect state distributions of a-Si:H and μc-Si:H layers of the tandem cell in the simulations are shown in Figure 7.2.

TABLE 7.1: Input parameters of the baseline a-Si:H and μc-Si:H p-i-n structures used in the simulations

Parameters	**a-Si:H p-layer**	**a-Si:H i-layer**	**a-Si:H n-layer**	**μc-Si:H p-layer**	**μc-Si:H i-layer**	**μc-Si:H n- layer**
Layer thickness, L(nm)	variable	variable	variable	variable	variable	variable
Dielectric constant	11.9	11.9	11.9	11.9	11.9	11.9
Bandgap, Eg (eV)	variable	variable	variable	variable	variable	variable
Electron mobility,	20	20	20	50	50	50
Hole mobility	5	5	5	5	5	5
Acceptor concentration, Na(cm-3)	variable	0	0	variable	0	0
Donator concentration, Nd (cm-3)	0	1000	variable	0	1000	variable
Effective DOS conduction Band, Nc (cm-3)	1.00E+20	1.00E+20	1.00E+20	1.00E+19	1.00E+19	1.00E+19
Effective DOS valence Band, Nv (cm-3)	1.00E+20	1.00E+20	1.00E+20	1.00E+19	1.00E+19	1.00E+19
Electron affinity (eV)	3.9	3.9	3.9	3.9	3.9	3.9
Valence Band tail states parameters						
VB trap density (cm-3)	2.40E+20	9.40E+19	1.88E+20	2.40E+20	9.40E+19	1.88E+20
VB tail characteristic energy (meV)	120	50	94	120	30	94
Electron capture cross section (cm2)	7.00E-16	7.00E-16	7E-16	7.00E-16	7.00E-16	7.00E-16
Hole capture cross section (cm2)	7.00E-16	7.00E-16	7E-16	7.00E-16	7.00E-16	7.00E-16
Conduction Band tail states parameters						
CB trap density (cm-3)	1.60E+20	6.40E+19	1.36E+20	2.40E+20	6.40E+19	1.36E+20
CB tail characteristic energy (meV)	80.00	35.00	68.00	80.00	20.00	68.00
Electron capture cross section (cm2)	7.00E-16	7.00E-16	7.00E-16	7.00E-16	7.00E-16	7.00E-16
Hole capture cross section (cm2)	7.00E-16	7.00E-16	7.00E-16	7.00E-16	7.00E-16	7.00E-16
Gaussian defect states parameters (Acceptor)						
Defect density (cm-3)	6.90E+19	5.00E+15	6.9E+19	6.90E+19	1.00E+15	6.90E+19
Standard deviation (Gaussian) (eV)	0.21	0.144	0.21	0.21	0.144	0.21
Electron capture cross section (cm2)	3.00E-15	3.00E-15	3.00E-15	3.00E-15	1.00E-15	3.00E-15
Hole capture cross section (cm2)	3.00E-14	3.00E-14	3.00E-14	3.00E-14	1.00E-14	3.00E-14
Gaussian defect states parameters (Donator)						
Defect density (cm-3)	6.90E+19	5.00E+15	6.9E+19	6.90E+19	1.00E+15	6.90E+19
Standard deviation (Gaussian) (eV)	0.21	0.144	0.21	0.21	0.144	0.21
Electron capture cross section (cm2)	3.00E-14	3.00E-15	3.00E-14	3.00E-14	1.00E-14	3.00E-14
Hole capture cross section (cm2)	3.00E-15	3.00E-14	3.00E-15	3.00E-15	1.00E-15	3.00E-14

Input parameters of the baseline a-Si:H and μc-Si:H p-i-n structures used in the simulations are given in Table 7.1. Unless otherwise stated in Table 7.1, all the default values of AFORS-HET were adopted. It is here to be noted that the basic parameters shown in Table 7.1 are taken from standard references [15, 99, 115].

According to density of state model, both amorphous and microcrystalline silicon contain acceptor-like states above the mid gap and donor-like states below the mid gap. This is because of the dangling bonds or defects introduced at the outer part of the crystal lattice and grain boundaries [14]. However, microcrystalline silicon shows somehow lower effective conduction band density (N_c) and valence band density (N_v). This is because of the crystalline grains presence in the material. That is why values of N_c and N_v are kept one order lower than that of amorphous silicon. Because of the same reason electron mobility and hole mobility are kept little higher.

The efficiency, short circuit current density, open circuit voltage, and fill factor of the micromorph device depend on design parameters like window layer thickness, donor and acceptor concentrations, electron and hole mobility, band-gap, and band-tail states. However, both amorphous and microcrystalline silicon have low mobility and large number of localized gap states which reduces the efficiency significantly. In this work, the input parameters like layer thickness, bandgap, donor and acceptor concentrations are varied to find best performed cell structure. Later on the performance of the optimized micromorph tandem cell is simulated and discussed.

7.2 Results and Discussions

7.2.1 Optimization of layer thickness

Layer thickness plays an important role in the optimization of a micromorph device. As p-layer is actually the window layer, its thickness is varied from 1nm - 100 nm in both amorphous and micocrystalline cells. Because of the indirect bandgap property of μc-Si:H it is essential to have a thick intrinsic layer for better absorption of photons which is not the case for amorphous intrinsic layer. Therefore, μc-Si:H i-layer is varied from several nanometers to 10 micrometers and a-Si:H i-layer is varied from several nanometers to 5 micrometers. The n-layers are kept within the 100 nm range and varied to find the optimum thickness for better electron transport.

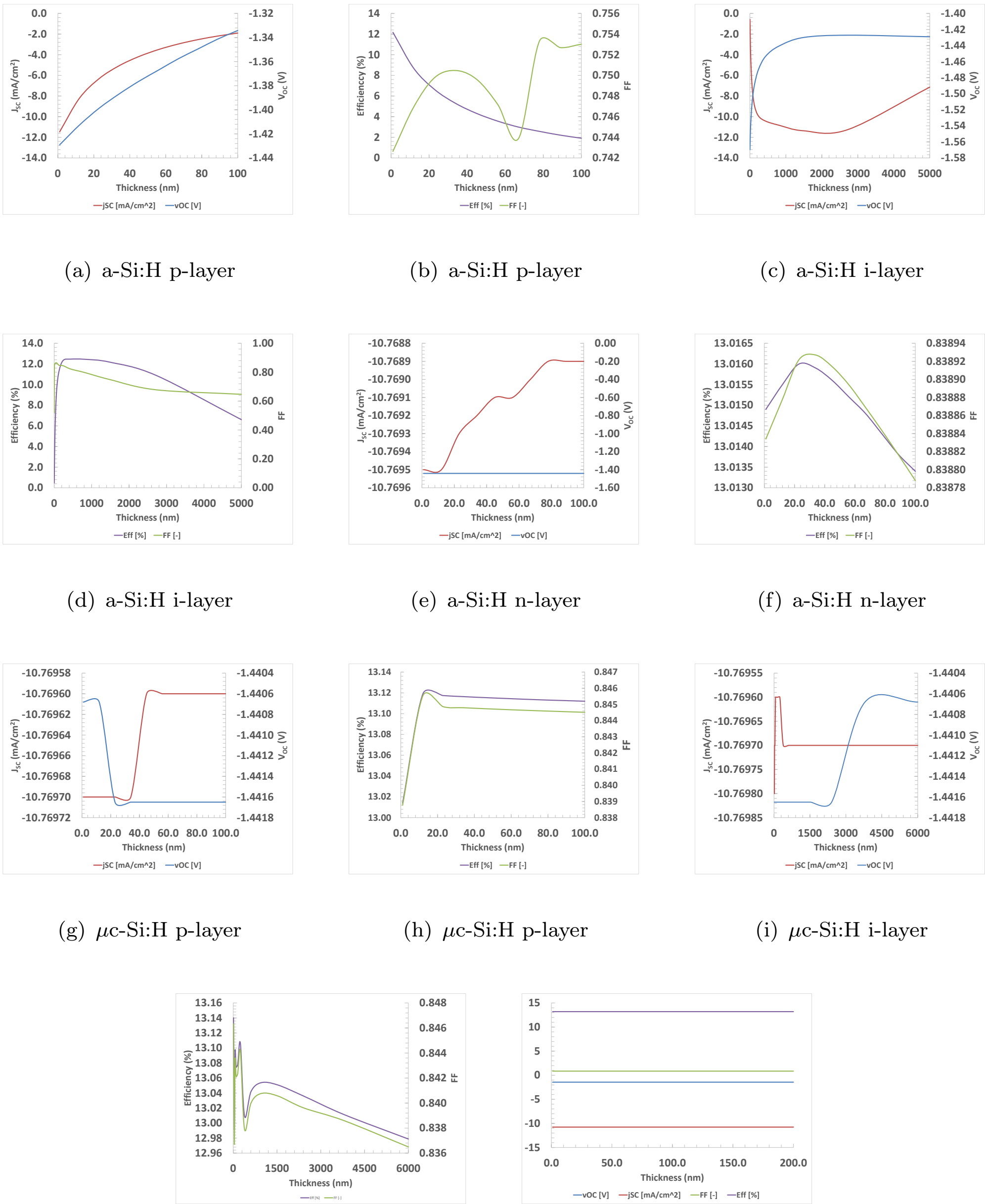

(a) a-Si:H p-layer (b) a-Si:H p-layer (c) a-Si:H i-layer

(d) a-Si:H i-layer (e) a-Si:H n-layer (f) a-Si:H n-layer

(g) μc-Si:H p-layer (h) μc-Si:H p-layer (i) μc-Si:H i-layer

(j) μc-Si:H i-layer (k) μc-Si:H n-layer

FIGURE 7.3: Effect of thickness variation on J_{SC} and V_{OC} are shown in (a), (c), and (e) for a-Si:H p-, i-, and n-layer respectively and in (g), (i), and (k) for μc-Si:H p-, i-, and n-layer respectively. Variation in efficiency and FF are shown in (b), (d), and (f) for a-Si:H p-, i-, and n-layer respectively and in (h), (j), and (k) for μc-Si:H p-, i-, and n-layer respectively.

Figure 7.3 illustrates the effect of thickness variation on J_{SC}, V_{OC}, FF, and Efficiency. From figure 7.3 (a) and 7.3 (b) it is evident that a thin a-Si:H p-layer of 1 to 5 nm would result in a better J_{SC}, and V_{OC}, and thus a higher efficiency. With increase in thickness of p-layer the amount of light reaching the absorber layer reduces and results in lower J_{SC} values. It also becomes difficult for the built in field to separate the electron-hole pair if the thickness of p-layer is high.

On the other hand, from figure 7.3 (c) and 7.3 (d) it can be seen that an a-Si:H absorber layer of 300 to 500 nm should be used to get better performance from the device. With increase of i-layer thickness J_{SC} increases gradually up to 2 μm but starts decreasing after that. However, V_{OC} decreases abruptly just after 300 nm and reaches to its minimum value after 1 μm.

For a-Si:H n-layer the maximum efficiency can be achieved within 20 to 30 nm range where efficiency and FF are maximum as shown in figure 7.3 (e) and 7.3 (f). Although J_{SC} decreases with increase of thickness V_{OC} remains constant throughout the variation. This is because of the lower electron and hole mobility of the a-Si:H where thicker n-layers reduces the electron transport facility.

From figure 7.3 (g) and 7.3 (h) it can be seen that for μc-Si:H p-layer thickness both J_{SC} and V_{OC} are maximum in 10 to 20 nm range. Thus efficiency and fill factor are also maximum within that range. As the thickness increases further the J_{SC} drops and efficiency also decreases.

Figure 7.3 (i) and 7.3 (j) illustrates the effects of μc-Si:H i-layer thickness variation. As an indirect semiconductor the μc-Si:H should have a thicker absorber layer to absorb as much photons as possible. However, increasing the thickness beyond 1.5 μm does not increase the efficiency anymore and the device reaches its saturation.

From figure 7.3 (k) it can be seen that variation of n-layer thickness has insignificant effect on J_{SC}, V_{OC}, FF, and efficiency. This might be because of the small number of photons reaching the bottom layer and lower electron and hole mobility of the μc-Si:H.

7.2.2 Optimization of doping concentration

Variation of efficiency along with J_{SC}, V_{OC}, and FF are depicted in figure 7.4 for the variation in acceptor and donor concentration. From figure 7.4 (a) it can be seen that V_{OC} and J_{SC} both increases with increase in a-Si:H p-layer acceptor concentration, N_a. However, beyond the acceptor concentration of $10^{19}cm^{-3}$ the V_{OC} and J_{SC} both reached

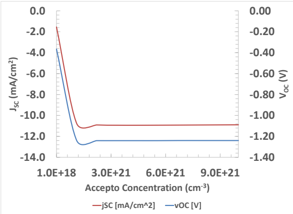

(a) Effect of a-Si:H p-layer N_a variation on J_{SC} and V_{OC}

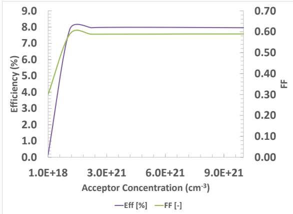

(b) Effect of a-Si:H p-layer N_a variation on Efficiency and FF

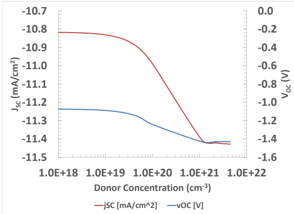

(c) Effect of a-Si:H n-layer N_d variation on J_{SC} and V_{OC}

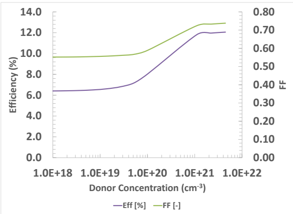

(d) Effect of a-Si:H n-layer N_d variation on Efficiency and FF

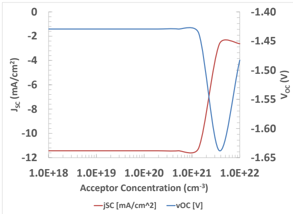

(e) Effect of μc-Si:H p-layer N_a variation on J_{SC} and V_{OC}

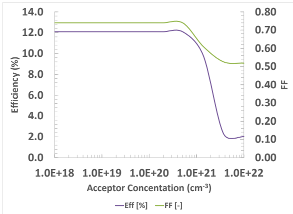

(f) Effect of μc-Si:H p-layer N_a variation on Efficiency and FF

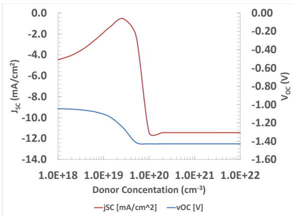

(g) Effect of μc-Si:H n-layer N_d variation on J_{SC} and V_{OC}

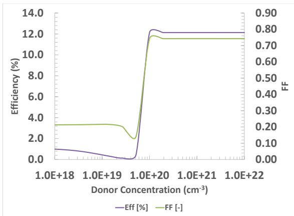

(h) Effect of μc-Si:H n-layer N_d variation on Efficiency and FF

FIGURE 7.4: Impact of Acceptor concentration (N_a) and Donor concentration (N_d) variation on J_{SC}, V_{OC}, Efficiency and FF.

the maximum value and do not increase further. This is because of the fully crowded states in the cell which saturates the performance. Because of this reason it is also seen from figure 7.4 (b) that efficiency and FF also reached to saturation after the $10^{19}cm^{-3}$ limit.

In the case of a-Si:H n-layer donor concentration, N_d from figure 7.4 (c) and 7.4 (d) it can be seen that V_{OC} and J_{SC} both do not increase till $10^{19}cm^{-3}$ but beyond that range V_{OC} and J_{SC} both increase rapidly up to $10^{21}cm^{-3}$ and then the device saturates. Increasing donor concentration further does not increase the efficiency and FF.

From figure 7.4(e) and 7.4(f) it can be seen that increasing μc-Si:H p-layer acceptor concentration up to $10^{21}cm^{-3}$ has no significant effect on both J_{SC} and V_{OC} and thus

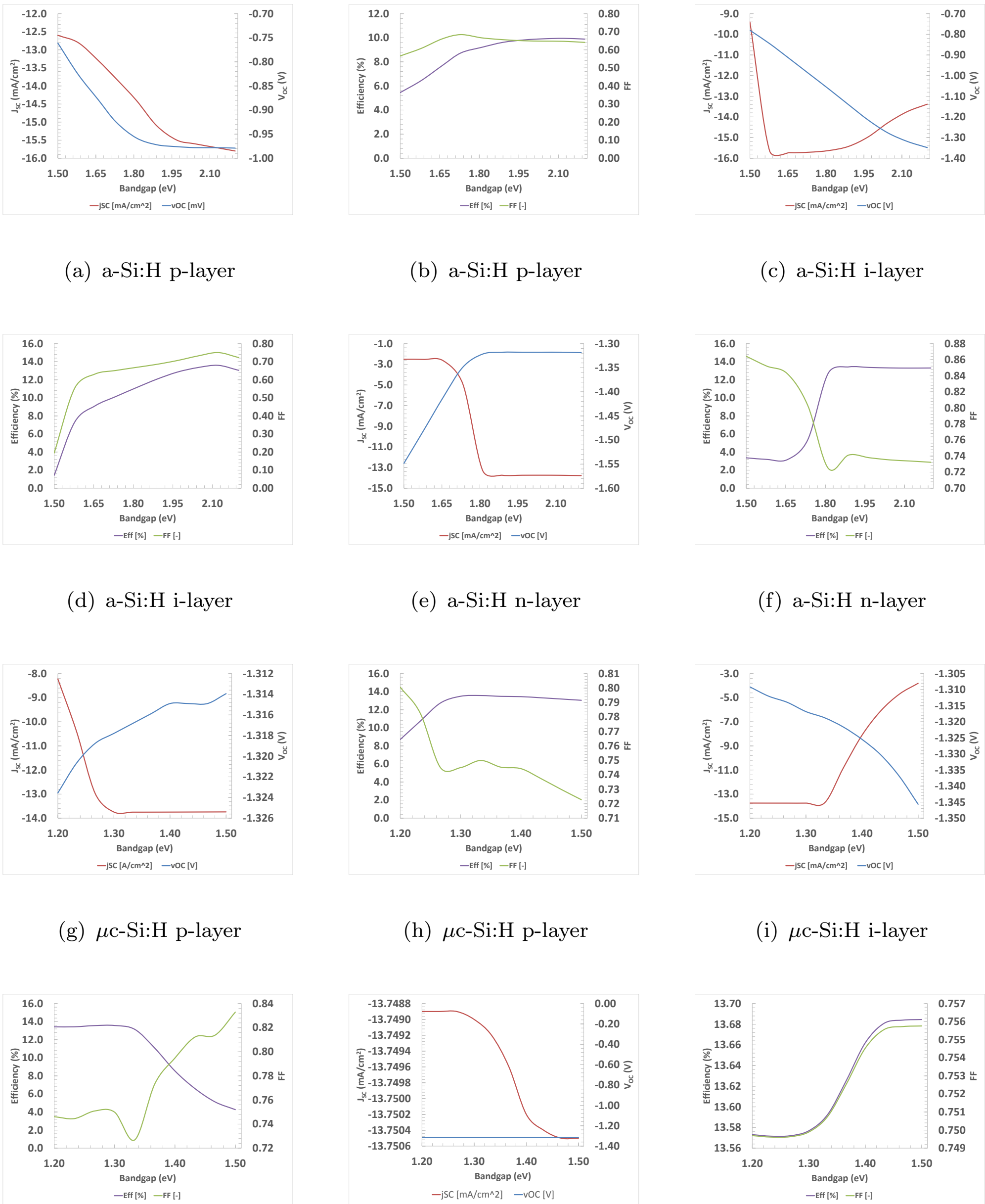

(a) a-Si:H p-layer (b) a-Si:H p-layer (c) a-Si:H i-layer

(d) a-Si:H i-layer (e) a-Si:H n-layer (f) a-Si:H n-layer

(g) μc-Si:H p-layer (h) μc-Si:H p-layer (i) μc-Si:H i-layer

(j) μc-Si:H i-layer (k) μc-Si:H n-layer (l) μc-Si:H n-layer

FIGURE 7.5: Effect of bandgap variation on J_{SC} and V_{OC} are shown in (a), (c), and (e) for a-Si:H p-, i-, and n-layer respectively and in (g), (i), and (k) for μc-Si:H p-, i-, and n-layer respectively. Variation in efficiency and FF are shown in (b), (d), and (f) for a-Si:H and (h), (j), and (l) for μc-Si:H p-, i-, and n-layers respectively.

efficiency and FF also remain almost constant for that range. However, increasing the acceptor concentration further reduces J_{SC} abruptly with very little increase in V_{OC}. Therefore, efficiency and fill factor both reduced as the device already reached its saturation.

In the case of μc-Si:H n-layer donor concentration variation- increasing the concentration from $10^{19} cm^{-3}$ to $10^{20} cm^{-3}$ increases the J_{SC} from 1 mA/cm^2 to 12 mA/cm^2 as shown in figure 7.4(g). V_{OC} also increases with increase in donor concentration. However, beyond $10^{20} cm^{-3}$ donor concentration the device is saturated and no further increase in either efficiecny or fill factor can be seen as shown in figure 7.4(h).

7.2.3 Optimization of Bandgap

Bandgaps of the p-, i-, and n-layers of both a-Si:H top cell and μc-Si:H bottom cell are varied to find the optimum bandgap for the micromorph device. For a-Si:H the bandgap can be varied from 1.5 to 2.2 eV and for μc-Si:H from 1.2 eV to 1.5 eV [1, 100]. The bandgaps of p-, i-, and n-layers were varied in the specified range for optimization. Effect of bandgap variation on J_{SC} and V_{OC}, efficiency and FF are shown in figure 7.5 for p-, i-, and n-layers of both amorphous and microcrystalline top and bottom cell. It can be seen from figure 7.5(a) and 7.5(b) that J_{SC} and V_{OC} both reaches to its maximum value with a higher bandgap of the a-Si:H window layer close to 2.1 eV. This is because with increase in p-layer bandgap more photons can reach the absorber layer to produce more current. It can also be seen that the V_{OC} also follows the similar trend. The reason why V_{OC} also increases can be the lower rate of recombination with higher badgap of window layer. Therefore, both efficiency and FF also reached their maximum value above 2.0 eV bandgap of p-layer.

For a-Si:H i-layer bandgap variation from 1.5 eV to 2.2 eV it can be seen from figure 7.5 (c) and (d) that J_{SC} increases abruptly with increase in i-layer bandgap from 1.5 eV to 1.6 eV. However, it starts to decrease after 1.8 eV. On the other hand, V_{OC} has an approximately linear increasing trend with increase in bandgap. This might be because of the lowering of band offset with increase in bandgap of i-layer. As bandgap of p-layer is kept at 2.1 eV, the low bandgap of i-layer would create a band offset which will eventually increase the recombination. Therefore maximum efficiency is achieved within the 2.0 to 2.1 eV range.

From figure 7.5(e) and 7.5(f) it can be seen that J_{SC} does not increase significantly with increase of a-Si:H n-layer bandgap from 1.5 to 1.65 eV but it increases abruptly after 1.65 eV and reaches saturation at around 1.80 eV. However, V_{OC} shows a opposite trend where it decreases continuously from bandgap variation from 1.5 to 1.8 eV but

Table 7.2: Optimum parameters found in the simulation and used to design the best-performed cell

Layers	Thickness, L(nm)	N_a (cm^{-3})	N_d (cm^{-3})	Eg (eV)
a-Si:H p-layer	1.12	4.41E+21	0	2.2
a-Si:H i-layer	500	0	1000	2.2
a-Si:H n-layer	23	0	8.00E+21	2.2
μc-Si:H p-layer	12	1.00E+18	0	1.5
μc-Si:H i-layer	1300	0	1000	1.2
μc-Si:H n-layer	20	0	1E+20	1.5

that decrease is not significant compared to the increase in J_{SC}. Therefore maximum efficiency is achieved close to the a-Si:H n-layer bandgap of 1.8 eV.

In the case of μc-Si:H p-layer bandgap variation it is evident from figure 7.5(g) and 7.5(h) that J_{SC} increases with increase of bandgap from 1.2 eV to 1.3 eV but V_{OC} deceases at the same time. However, maximum efficiency is achieved with bandgap of around 1.3 eV but with little lower FF of about 0.74.

In figure 7.5(i) and 7.5(j) the effect of bandgap variation of μc-Si:H i-layer is illustrated. It can be seen from the plots that J_{SC} remained almost constant from 1.2 to 1.35 eV after which it decreased rapidly. Although V_{OC} increases with increase of bandgap the increase is not significant compared to the decrease of J_{SC}. Therefore, the maximum efficiency is achieved with bandgap of 1.35 eV.

Finally, in figure 7.5(k) and 7.5(l) the effect of bandgap variation of μc-Si:H n-layer is given. It is evident from the graphs that V_{OC} remains almost constant throughout the variation of bandgap. However, J_{SC} increases with increase of n-layer bandgap. The maximum efficiency and FF are achieved with a higher bandgap close to 1.4 eV.

7.2.4 Design optimized solar cell performance

By taking all the optimal values of the layer thicknesses, bandgap, and doping concentrations of both a-Si:H top cell and μc-Si:H bottom cell and running the simulation using AFORS-HET the characteristics of the best performed cell was found. Table 7.2 shows the optimum parameters found in the simulation and used to design the best-performed micromorph cell.

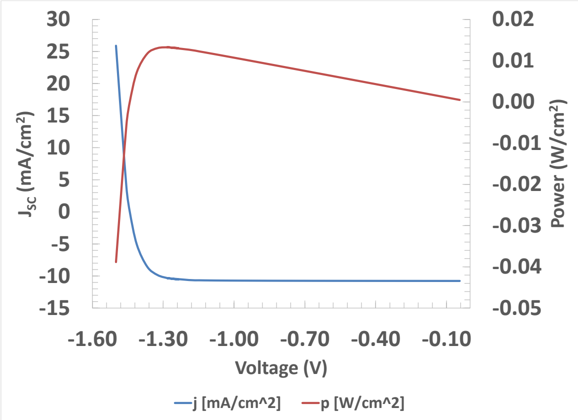

FIGURE 7.6: J-V and P-V curve of the best performed micromorph cell under AM 1.5 and 1000 W/m^2 illumination

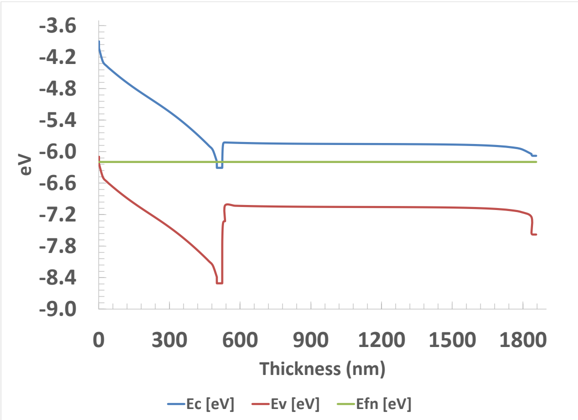

FIGURE 7.7: Band diagram of the optimum cell under equilibrium condition

Illumination of 1000 W/m^2 at AM 1.5 was used to find the J-V and P-V curves shown in figure 7.6. The calculated light J-V characteristics of the cell yield the following results:

Short circuit current density of J_{SC} = -10.77 mA/cm^2,

Open circuit voltage V_{OC} = -1442 mV ,

Fill-factor, FF = 0.853,

Efficiency = 13.25 %.

Figure 7.7 shows the band diagram of the optimum tandem cell under equilibrium condition. The fermi level was found to be at -6.2 eV. The generation and recombination

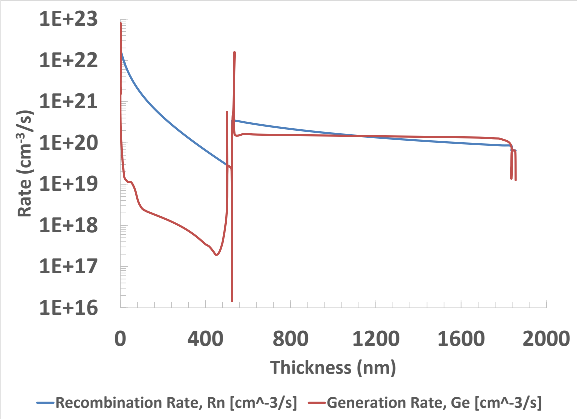

Figure 7.8: Generation and recombination rate of the best performed cell

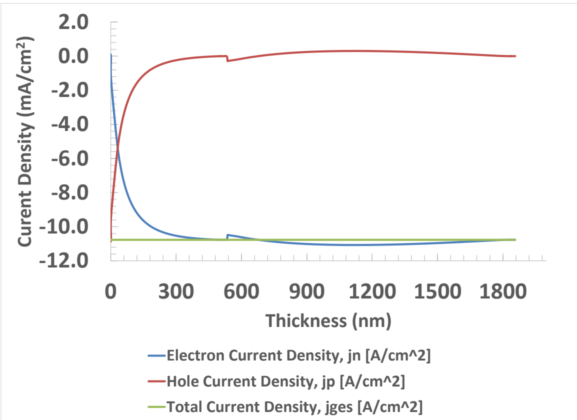

Figure 7.9: Current density of the micromorph tandem cell

rate of the designed cell is illustrated in figure 7.8. It can be seen that the recombination rate is much higher at the front surface of the cell. In the bottom cell generation and recombination is almost equal which questions the use of bottom cell. This is because of current mismatch of the device which initiates the necessity of intermediate reflectors in between the top and bottom cell. Besides this, front surface recombination can be reduced by adding surface passivation to the layer.

Figure 7.9 shows the electron and hole current densities with the variation of thickness of the device. The total output current density remained at around -10.77 mA/cm^2 which is pretty high for a micromorph tandem cell. This indicates that a well-designed tandem cell can have a higher current density and better performance.

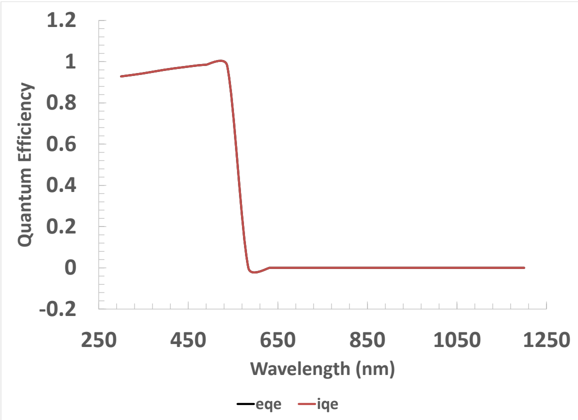

FIGURE 7.10: Internal and external quantum efficiency of the micromorph cell

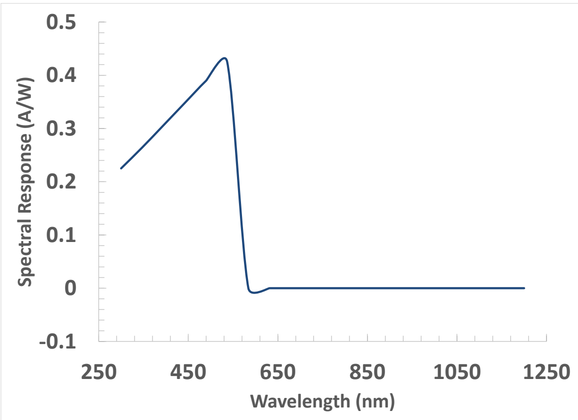

FIGURE 7.11: Spectral response of the optimal micromorph tandem cell

Figure 7.10 illustrates the internal and external quantum efficiencies of the cell. The external quantum efficiency reached a maximum of 98.48% at wavelength (λ) of 490 nm. The overall external quantum efficiency remained very high from 90-98 % for wavelength of 300-550 nm range. This indicates that the tandem micromorph device is top cell limited and will perform its best under ultra-violet and near visible light wavelengths. Figure 7.11 shows the spectral response of the cell which also indicates the similar scenario.

7.3 Conclusions

With AFORS-HET simulation software, the parameters like bandgap, layer thickness, and doping concentrations of both a-Si:H top cell and μc-Si:H bottom cell are varied. From the simulation it is found that layer thicknesses have significant effects on efficiency improvement. For the a-Si:H top cell, a thin a-Si:H p-layer of 1 to 5 nm would result in a better J_{SC}, and V_{OC}, and thus a higher efficiency. Although in a micromorph concept the amorphous absorber layer should be as thin as possible but i-layer thickness should be in the range of 400-500 nm for the top cell. A thin n-layer of around 20 nm is necessary for a-Si:H top cell to have higher efficiency. For the μc-Si:H bottom cell, the similar trend is also true. A thin p-layer followed by a much thicker i-layer of around 1000 to 1500 nm and then a thin n-layer of 20 nm will give better efficiency and performance for the micromorph device. The doping concentrations of p-, and n-layers of both top and bottom cells are also varied and maximum efficiency of around 13.25% is achieved with top cell acceptor concentration of $4.41 \times 10^{21} cm^{-3}$ and donor concentration of $8 \times 10^{21} cm^{-3}$ and bottom cell acceptor concentration of $1 \times 10^{18} cm^{-3}$ and donor concentration of $1 \times 10^{20} cm^{-3}$. The bandgap of p-, i-, and n-layer of both top and bottom cells are also varied and optimum performance is found at higher bandgaps closer to 2.2 eV for a-Si:H top cell and 1.5 eV for μc-Si:H bottom cell.

Finally, using these values an optimum cell is numerically designed and simulated. It is found that the best-performed cell has a short circuit current density of -10.77 mA/cm^2, open circuit voltage of -1442 mV, fill factor of 0.853, and efficiency of 13.25%. The cell has higher front surface recombination speeds which can be reduced by surface passivation. As the designed micromorph tandem cell is top cell limited intermediate reflectors should be used to further improve the performance of the device. The quantum efficiency and spectral response curves also showed that the cell has a very good spectral response in the 300-550 nm range.

Chapter 8

Conclusion and Discussion

8.1 Comparative analysis

The study, optimization, and simulation of a hydrogenated amorphous silicon p-i-n cell is done in chapter 4. It is found that the best efficiency of this numerically designed single junction aSi:H solar cell is 13.26% with intrinsic layer thickness of 1600 nm and optimum window layer bandgap of 2.17 eV.

In chapter 5, it is shown that the numerically designed optimum μc-Si:H p-i-n cell has a short circuit current density of -33 mA/cm^2, open circuit voltage of -906.5 mV, fill factor of 0.694, and efficiency of 20.78%.

From chapter 6, it is found the best-performed micromorph cell has a short circuit current density of -10.77 mA/cm^2, open circuit voltage of -1442 mV, fill factor of 0.853, and efficiency of 13.25%.

The comparative values of J_{SC}, V_{OC}, FF, and efficiencies of all the numerically designed cells and conventional c-Si p-n cell are given in table 8.1. From the table it is evident that μc-Si:H p-i-n cell has the highest conversion efficiency compared to a-Si p-i-n and micromorph tandem cell. Maximum short circuit current density is also achieved by the μc-Si:H p-i-n cell. The micromorph tandem cell has the lowest short circuit current density compared to other cells. The value of V_{OC} is minimum for μc-Si:H p-i-n cell and maximum for micromorph tandem cell. In case of fill factor the micromorph tandem cell is the best which has a fill factor of 0.853. However, the single junction p-i-n cells

TABLE 8.1: Comparative values of J_{SC}, V_{OC}, FF, and efficiencies of all the numerically designed cells

Type of cell	$\mathbf{J_{SC}}$ **(mA/cm^2)**	$\mathbf{V_{OC}}$ **(V)**	**FF**	**Efficiecny (%)**
a-Si:H p-i-n cell	-19.87	-0.9670	0.6890	13.26
μc-Si:H p-i-n cell	-33.00	-0.9065	0.6940	20.78
micromorph tandem cell	-10.77	-1.4420	0.8530	13.25
conventional c-Si cell	45.37	0.6994	0.8427	26.74

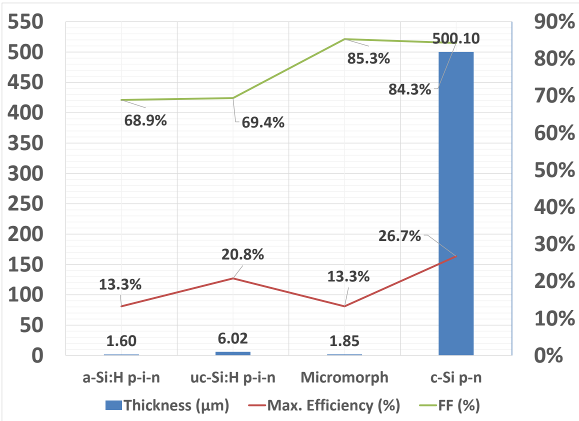

FIGURE 8.1: Comparative thickness, efficiency, and FF of a-Si:H p-i-n, μc-Si p-i-n, micromorph tandem, and conventional c-Si cell

have almost similar and low FF close to 0.69. Compared to conventional p-n junction cell almost all the parameters of the thin-film cells are low except the V_{OC} of tandem micomorph cell. Efficiency of the numerically designed cells are also low compared to conventional c-Si cell. However, from figure 8.1 it can be seen that conventional c-Si cell requires a very high thickness close to 500 μm whereas, the numerically designed cells require a thickness not more than 6 μm. If the high thickness of conventional c-Si and its associated costs are taken into consideration then thin-film p-i-n cells or micromorph tandem cells have a way better prospect in PV industry.

Figure 8.2 illustrates the external quantum efficiencies of a-Si:H p-i-n, μc-Si p-i-n, micromorph tandem, and conventional c-Si cell. It can be seen from the plot that compared to conventional c-Si PV cell thin-film a-Si:H p-i-n, μc-Si p-i-n, and micromorph tandem cells have better short wavelength efficiency. These numerically designed cells can perform very well in high frequency spectrum. Micromorph tandem structure and a-Si:H p-i-n cell have highest external quantum efficiencies in the 300-500 nm range. Although, μc-Si p-i-n has a comparatively lower external quantum efficiency in the 300-500 nm range but

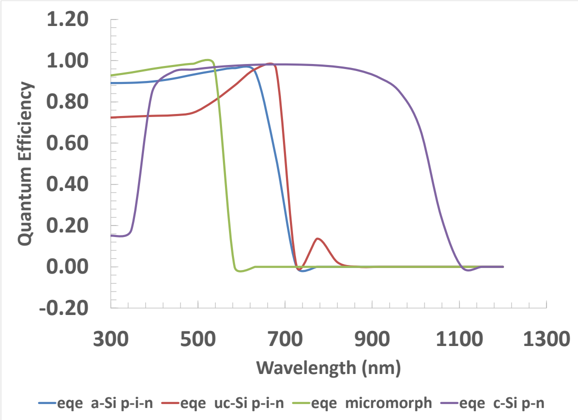

Figure 8.2: External quantum efficiency curves of a-Si:H p-i-n cell, μc-Si p-i-n cell, micromorph tandem cell, and conventional c-Si cell

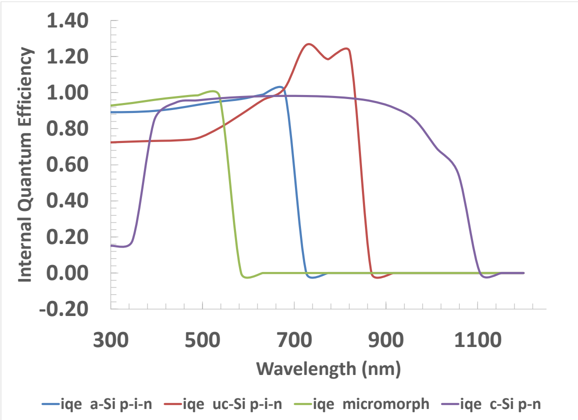

Figure 8.3: Internal quantum efficiency curves of a-Si:H p-i-n cell, μc-Si p-i-n cell, micromorph tandem cell, and conventional c-Si cell

it is much higher compared to conventional c-Si cell. For the midrange wavelengths i.e. from 600-800 nm range, conventional c-Si cell perform best. Among the numerically designed thin-film cells μc-Si p-i-n cell perform better in this range of wavelengths. Almost all the numerically designed cells have zero external quantum efficiency in the 800-1200 nm range i.e. infrared range. The internal quantum efficiency curves also show the same trend as shown in figure 8.3.

The spectral response curves of conventional c-Si PV cell along with numerically designed p-i-n cells and micromorph tandem cell are shown in figure 8.4. At short wavelengths, each photon has a large energy, and hence the ratio of photons to power is reduced.

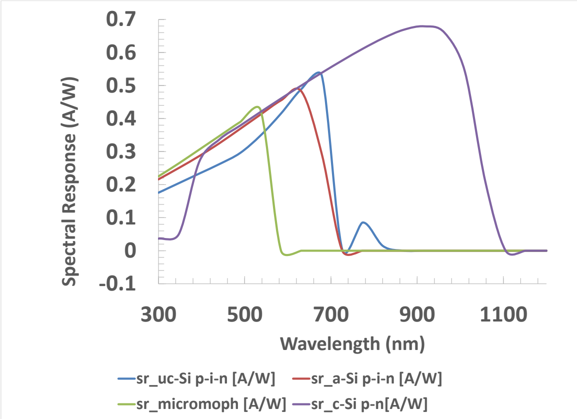

FIGURE 8.4: Spectral responses of a-Si:H p-i-n cell, μc-Si p-i-n cell, micromorph tandem cell, and conventional c-Si PV cell

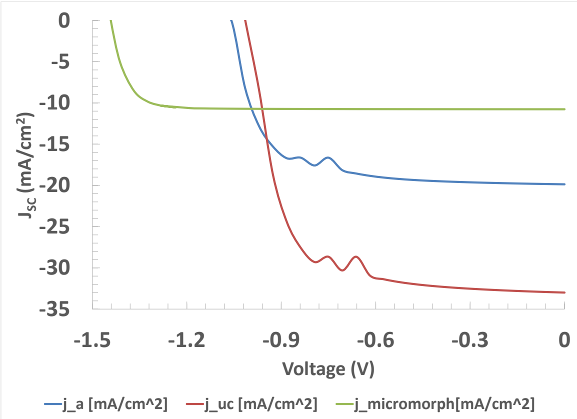

FIGURE 8.5: Comparative J-V curves of a-Si:H p-i-n cell (j_a), μc-Si p-i-n cell (j_uc), and micromorph tandem cell (j_micromorph)

Therefore, any energy above the band gap energy is not utilized by the solar cell and instead goes to heating the solar cell. The inability of the conventional c-Si solar cell to convert high energy photons to electricity introduces high temperature of the PV panel which reduces efficiency further. Interestingly, the numerically designed p-i-n cells and micromorph tandem can utilize the high frequency portion of the spectrum and eliminate this problem of over heating of the panels.

Comparative J-V curves of a-Si:H p-i-n cell, μc-Si p-i-n cell, and micromorph tandem cell are shown in figure 8.5. The P-V curves are shown in figure 8.6. From both of the graphs it is easily understood that the μc-Si:H p-i-n cell is the most efficient with high power

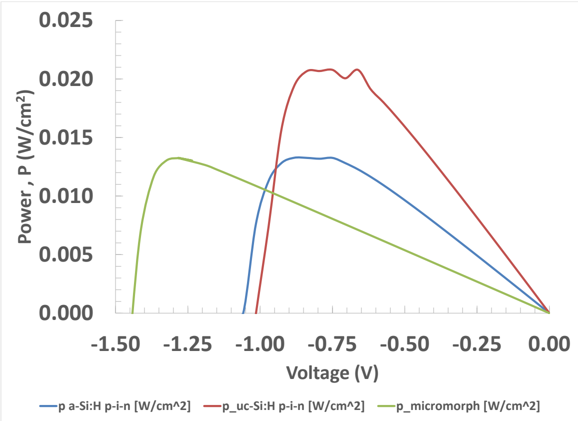

FIGURE 8.6: Comparative P-V curves of a-Si:H p-i-n cell, μc-Si p-i-n cell, and micromorph tandem cell

output. However, it has a lower fill factor and open circuit voltage. On the other hand, micromorph tandem solar cell has higher open circuit voltage and fill factor but lower short circuit current. Therefore, for higher open circuit voltage requirement micromorph tandem structure should be preferred. Amorphous single junction p-i-n cell is also a good candidate for thin-film silicon solar cell but because of its SWE degradation it is not a very good choice. Therefore, it can be concluded from this study that among all the numerically designed cells μc-Si:H p-i-n cell is the best choice because of its high short circuit current density, moderate open circuit voltage, and fill factor.

8.2 Scope of future work

Further work can be done to numerically design heterostructure solar cells like a-Si:H p- a-Si:H i- μc-Si:H n heterostructure cell. The n-i-p structure can also be investigated. Organic and inorganic hybrid solar cell can be a very good option to reduce the SWE degradation of thin-film PV cell. Numerical design and fabrication of such PV cell could be good future work. The effect of intermediate reflector to reduce a-Si:H layer thickness can also be investigated for a-Si:H p-i-n cell and micromorph tandem cell. Use of ZnO layer as an intermediate reflector can be simulated to see the effects. Voltage and current matching problems of micromorph tandem cell can be further researched for a better solution.

8.3 Conclusion

With AFORS-HET simulation software, the design parameters like bandgap, layer thickness, and doping concentrations of a-Si:H p-i-n cell, μc-Si:H p-i-n cell, and micromorph tandem solar cells have been varied to optimize their performance. The efficiency of a single junction a-Si:H p-i-n cell can be achieved up to 13.26% with optimized window layer band-gap of around 2 eV and the short circuit current density is 19.87mA/cm2, open circuit voltage is 0.967 volts and fill factor is 0.689. The numerically designed optimum μc-Si:H p-i-n cell has a short circuit current density of -33 mA/cm2, open circuit voltage of -906.5 mV, fill factor of 0.694, and efficiency of 20.78%. Finally, it is also found that the best-performed micromorph tandem cell has a short circuit current density of -10.77 mA/cm2, open circuit voltage of -1442 mV, fill factor of 0.853, and efficiency of 13.25%. Compared to conventional c-Si PV cell, thin-film a-Si:H p-i-n, μc-Si p-i-n, and micromorph tandem cells have better short wavelength efficiency. These numerically designed cells can perform very well in high frequency spectrum. Micromorph tandem structure and a-Si:H p-i-n cell have highest external quantum efficiencies in the 300-500 nm range. Although, μc-Si p-i-n has a comparatively lower external quantum efficiency in the 300-500 nm range but it is much higher compared to conventional c-Si cell. For the midrange wavelengths i.e. from 600-800 nm range, μc-Si:H p-i-n cell perform better. Almost all the numerically designed cells have zero external quantum efficiency in the 800-1200 nm range i.e. in infrared range. The study also reveals that the μc-Si:H p-i-n cell is the most efficient but it has a lower fill factor and open circuit voltage. It can also be concluded that for higher open circuit voltage requirement micromorph tandem structure should be preferred.

Appendix A

Numerical Modeling of Solar Cell

With appropriate boundary conditions under steady-state conditions and under small sinusoidal perturbations, AFORS-HET can simulate one dimensional semiconductor structures by numerical methods [92]. To do this, the coupled partial differential equations set is transformed into non-linear algebraic equations set by finite difference methods. At bulk condition, the following one dimensional Poisson's equation and the transport equation for electrons and holes are solved:

$$\frac{\varepsilon_0\varepsilon_r}{q}\frac{\partial^2\phi(x,t)}{\partial x^2} = p(x,t) - n(x,t) + N_D - N_A + \sum_{defects}\rho_t(x,t) \tag{A.1}$$

$$-\frac{1}{q}\frac{\partial j_n(x,t)}{\partial x} = G_n(x,t) - R_n(x,t) - \frac{\partial}{\partial t}n(x,t) \tag{A.2}$$

$$\frac{1}{q}\frac{\partial j_p(x,t)}{\partial x} = G_p(x,t) - R_p(x,t) - \frac{\partial}{\partial t}p(x,t) \tag{A.3}$$

Where, n is the electron density, p is the hole density, and ϕ is the electric potential for which the system of differential equations is solved. q is the electron charge, ε_0, ε_r are the absolute and relative dielectric constants respectively, N_D, and N_A are the concentrations of donors and acceptors respectively. The distribution function f_t describes the charge stored in the defects, specifying the probability that defects with defect density N_t at the position E within the bandgap are occupied with electrons:

acceptor-type defect:

$$\rho_t(x,t) = -\int dE f_t(E,x,t) N_t(E) \tag{A.4a}$$

donor-type defect:

$$\rho_t(x,t) = \int dE(1 - f_t(E,x,t)) N_t(E) \tag{A.4b}$$

The electron current j_n, and hole current j_p are driven by the gradient of the corresponding quasi Fermi energy $E_{Fn,p}$ which is equivalent to the sum of a diffusion and a drift current with mobility μ_n, or μ_p within the bulk. This can be expressed as:

$$j_n(x,t) = q\mu_n n(x,t)\frac{\partial E_{Fn}(x,t)}{\partial x} = -\frac{\mu_n kT}{q}\frac{\partial n(x,t)}{\partial x} + \mu_n n(x,t)\frac{\partial \phi(x,t)}{\partial x} \tag{A.5a}$$

$$j_p(x,t) = q\mu_p p(x,t)\frac{\partial E_{Fp}(x,t)}{\partial x} = -\frac{\mu_p kT}{q}\frac{\partial p(x,t)}{\partial x} + \mu_p p(x,t)\frac{\partial \phi(x,t)}{\partial x} \tag{A.5b}$$

When the structure is illuminated, the super-bandgap optical generation rate (for $hc/\lambda \geq E_g$) from the valence band into the conduction band of semiconductor layers can be obtained by assuming simple Lambert-Beer absorption by specifying spectral absorption coefficient α of each layer. For sub-bandgap generation (for $hc/\lambda \leq E_g$) from a defect to conduction or valence band can be defined by specifying optical emission coefficients for the defect state:

$$e_n^0(E,x) = \sigma_n^0 N_C \Phi(\lambda,x)\vartheta(E_C - E - hc/\lambda) \tag{A.6a}$$

$$e_p^0(E,x) = \sigma_p^0 N_V \Phi(\lambda,x)\vartheta(E - E_V - hc/\lambda) \tag{A.6b}$$

Where, $e_n^0(E)$, $e_p^0(E) \neq 0$, and σ_n^0, σ_p^0 are the optical cross sections, $\Phi(\lambda, x)$ is the spectral photon flux, with wavelength λ at position x, N_C, and N_V are the conduction and valence band density respectively, and E_C, and E_V are the conduction and valence band energy respectively, and $\vartheta(E) = 1$ for $E \leq 0$, $\vartheta(E) = 0$ for $E > 0$.

Now, for the recombination from conduction band into valence band which might occur directly which is called band to band recombination, or Auger recombination. Recombination might also occur because of defects via trap states which is called Shockley-Read-Hall recombination or SRH recombination:

$$R_{n,p}(x,t) = R_{n,p}^{direct}(x,t) + R_{n,p}^{SRH}(x,t) \tag{A.7}$$

The detailed derivation of these recombinations can be found at [92–95]. Finally, for boundary conditions, the electrical potential of one contact is taken as zero and at the second contact a boundary condition is specified which relates the external cell voltage or current to internal quantities. For voltage controlled, Schottky contact [92]:

$$\varphi(0) = \phi_{front} - \phi_{back} + V_{ext} \qquad \varphi(L) = 0 \tag{A.8a}$$

$$j_n(0) = qS_n^{front}(n(0) - n_{eq}(0)) \qquad j_n(L) = -qS_n^{back}(n(L) - n_{eq}(L)) \tag{A.8b}$$

$$j_p(0) = qS_p^{front}(p(0) - p_{eq}(0)) \qquad j_p(L) = -qS_p^{back}(p(L) - p_{eq}(L)) \tag{A.8c}$$

Where, ϕ is the metal work function, S is the surface recombination velocity, n_{eq} or p_{eq} is the majority carrier density under equilibrium which can be found by the energy barrier of the metal or semiconductor contact, the corresponding minority carrier density by the mass action law: $n_{eq} = N_C e^{\frac{q\phi - q\chi}{kT}}$ or $p_{eq} = N_V e^{\frac{-(E_g - q\phi + q\chi)}{kT}}$, $n_{eq}p_{eq} = N_C N_V e^{\frac{-E_g}{2kT}}$.

For current controlled Schottky contact, the boundary condition for the external cell voltage is replaced by a condition for the external cell current:

$$j_n(0) + j_p(0) = j_{ext} \tag{A.9}$$

To simulate the deep dangling bond states two Gaussian distribution functions are modeled along with conduction and valence band tail states. .

Bibliography

[1] Wilfried van Sark, Lars Korte, and Francesco Roca. *Physics and technology of amorphous-crystalline heterostructure silicon solar cells.* Springer, 2012.

[2] R. S. Ohl. Light sensitive electric device, 1941.

[3] Robert A Street. *Hydrogenated amorphous silicon.* Cambridge University Press, 2005.

[4] Yoshihiro Hamakawa. *Thin-film solar cells: next generation photovoltaics and its applications*, volume 13. Springer Science & Business Media, 2013.

[5] Martin A Green, Keith Emery, Yoshihiro Hishikawa, Wilhelm Warta, and Ewan D Dunlop. Solar cell efficiency tables (version 45). *Progress in photovoltaics: research and applications*, 23(1):1–9, 2015.

[6] SJ Fonash. *Solar Cell Device Physics.* Academic Press, New York, USA, 2nd edition, 2010.

[7] Mokhtar Chahi, Ahmed Bouhekka, Jamal Dine Sib, Aissa Kebab, Yahya Bouizem, and Larbi Chahed. Optoelectronic properties simulation of hydrogenated microcrystalline silicon schottky diode. *physica status solidi (c)*, 7(3-4):640–645, 2010.

[8] S Vepřek and V Mareček. The preparation of thin layers of ge and si by chemical hydrogen plasma transport. *Solid-State Electronics*, 11(7):683–684, 1968.

[9] H Keppner, Johannes Meier, P Torres, D Fischer, and A Shah. Microcrystalline silicon and micromorph tandem solar cells. *Applied physics A*, 69(2):169–177, 1999.

[10] T Kilper, W Beyer, G Bräuer, T Bronger, R Carius, MN Van den Donker, D Hrunski, A Lambertz, T Merdzhanova, A Mück, et al. Oxygen and nitrogen impurities

in microcrystalline silicon deposited under optimized conditions: Influence on material properties and solar cell performance. *Journal of applied physics*, 105(7): 074509–074509, 2009.

[11] M Faraji, Sunil Gokhale, SM Choudhari, MG Takwale, and SV Ghaisas. High mobility hydrogenated and oxygenated microcrystalline silicon as a photosensitive material in photovoltaic applications. *Applied Physics Letters*, 60(26):3289–3291, 1992.

[12] J Meier, R Flückiger, H Keppner, and Arvind Shah. Complete microcrystalline p-i-n solar cellâĂŤcrystalline or amorphous cell behavior? *Applied Physics Letters*, 65(7):860–862, 1994.

[13] O Vetterl, F Finger, R Carius, P Hapke, L Houben, O Kluth, A Lambertz, A Mück, B Rech, and H Wagner. Intrinsic microcrystalline silicon: A new material for photovoltaics. *Solar Energy Materials and Solar Cells*, 62(1):97–108, 2000.

[14] Arvind Shah. *Thin-film silicon solar cells*. EPFL press, 2010.

[15] Mansi Sharma, Sushil Kumar, Neeraj Dwivedi, Sucheta Juneja, AK Gupta, S Sudhakar, and Kamlesh Patel. Optimization of band gap, thickness and carrier concentrations for the development of efficient microcrystalline silicon solar cells: A theoretical approach. *Solar Energy*, 97:176–185, 2013.

[16] Czang-Ho Lee, Myunghun Shin, Mi-Hwa Lim, Jun-Yong Seo, Jung-Eun Lee, Hee-Yong Lee, Byoung-June Kim, and Donguk Choi. Material properties of microcrystalline silicon for solar cell application. *Solar Energy Materials and Solar Cells*, 95 (1):207–210, 2011.

[17] Martin A Green. *Third generation photovoltaics*. Springer, 2006.

[18] David E Carlson and Cristopher R Wronski. Amorphous silicon solar cell. *Applied Physics Letters*, 28(11):671–673, 1976.

[19] A Bielawny, J Üpping, and RB Wehrspohn. Spectral properties of intermediate reflectors in micromorph tandem cells. *Solar Energy Materials and Solar Cells*, 93 (11):1909–1912, 2009.

[20] Gavin J. Conibeer and Arthur Willoughby. *Solar cell materials: developing technologies*. John Wiley & Sons, 2014.

[21] Walter R Runyan. *Silicon semiconductor technology*. McGraw-Hill, 1965.

[22] Adolf Goetzberger, Joachim Knobloch, and Bernhard Voss. Crystalline silicon solar cells. *editorial John Wiley & Sons Ltd*, 1, 1998.

[23] Robert Hull. *Properties of crystalline silicon*. Number 20. IET, 1999.

[24] Wolfgang Rainer Fahrner. *Amorphous silicon/crystalline silicon heterojunction solar cells*. Springer, 2013.

[25] J Springer, A Poruba, A Feifar, M Vanecek, N Wyrsch, L Feitknecht, J Meier, and A Shah. Nanotextured thin film silicon solar cells: optical model. In *16th EC Photovoltaic Solar Energy Conference*, number PV-LAB-CONF-2000-014, pages 434–437, 2000.

[26] Masanori Otobe and Shunri Oda. Preparation of microcrystalline silicon films by very-high-frequency digital chemical vapor deposition. *Japanese journal of applied physics*, 31(6S):1948, 1992.

[27] Tim Searle. Amorphous silicon and its alloys. *Inspec, IEE, London, UK*, 1998.

[28] Simon M Sze and Kwok K Ng. *Physics of semiconductor devices*. John wiley & sons, 2006.

[29] DL Staebler and CR Wronski. Reversible conductivity changes in discharge-produced amorphous si. *Applied physics letters*, 31(4):292–294, 1977.

[30] F Meillaud, E Vallat-Sauvain, X Niquille, M Dubey, J Bailat, A Shah, and C Ballif. Light-induced degradation of thin film amorphous and microcrystalline silicon solar cells. In *Conference Record of the Thirty-first IEEE Photovoltaic Specialists Conference, 2005.*, pages 1412–1415. IEEE, 2005.

[31] F Meillaud, E Vallat-Sauvain, Arvind Shah, and C Ballif. Kinetics of creation and of thermal annealing of light-induced defects in microcrystalline silicon solar cells. *Journal of Applied Physics*, 103(EPFL-ARTICLE-148391):054504, 2008.

[32] W De Soto, S A Klein, and W A Beckman. Improvement and validation of a model for photovoltaic array performance. *Solar Energy*, 80:78–88, 2006.

[33] C Carrero, J Amador, and S Arnaltes. A single procedure for helping pv designers to select silicon pv modules and evaluate the loss resistances. *Renewable Energy*, 32:2579–2589, 2007.

[34] Xavier Camps, Guillermo Velasco, Jordi de la Hoz, and Helena Martin. Contribution to the PV-to-inverter sizing ratio determination using a custom flexible experimental setup. *Applied Energy*, 149:35 – 45, 2015. ISSN 0306-2619. doi: http://dx.doi.org/10.1016/j.apenergy.2015.03.050.

[35] M. Eccher, A. Salemi, S. Turrini, and R.S. Brusa. Measurements of power transfer efficiency in CPV cell-array models using individual DC-DC converters. *Applied Energy*, 142:396 – 406, 2015. ISSN 0306-2619. doi: http://dx.doi.org/10.1016/j.apenergy.2014.12.038.

[36] Boualem Bendib, Hocine Belmili, and Fateh Krim. A survey of the most used MPPT methods: Conventional and advanced algorithms applied for photovoltaic systems. *Renewable and Sustainable Energy Reviews*, 45:637 – 648, 2015. ISSN 1364-0321. doi: http://dx.doi.org/10.1016/j.rser.2015.02.009.

[37] Kashif Ishaque, Zainal Salam, and George Lauss. The performance of perturb and observe and incremental conductance maximum power point tracking method under dynamic weather conditions. *Applied Energy*, 119:228 – 236, 2014. ISSN 0306-2619. doi: http://dx.doi.org/10.1016/j.apenergy.2013.12.054.

[38] Javad Khazaei, Zhixin Miao, Lakshan Piyasinghe, and Lingling Fan. Real-time digital simulation-based modeling of a single-phase single-stage PV system. *Electric Power Systems Research*, 123:85 – 91, 2015. ISSN 0378-7796. doi: http://dx.doi.org/10.1016/j.epsr.2015.01.023.

[39] P. Sivakumar, Abdullah Abdul Kader, Yogeshraj Kaliavaradhan, and M. Arutchelvi. Analysis and enhancement of PV efficiency with incremental conductance mppt technique under non-linear loading conditions. *Renewable Energy*, 81:543 – 550, 2015. ISSN 0960-1481. doi: http://dx.doi.org/10.1016/j.renene.2015.03.062.

[40] Valerio Lo Brano, Aldo Orioli, Giuseppina Ciulla, and Alessandra Di Gangi. An improved five-parameter model for photovoltaic modules. *Solar Energy Materials & SolarCells*, 94:1358–1370, 2010.

[41] Valerio Lo Brano, Aldo Orioli, and Giuseppina Ciulla. On the experimental validation of an improved five-parameter model for silicon photovoltaic modules. *Solar Energy Materials & SolarCells*, 105:27–39, 2012.

[42] D. Sera, R. Teodorescu, and P. Rodriguez. PV panel model based on datasheet values. In *Industrial Electronics, 2007. ISIE 2007. IEEE International Symposium on*, pages 2392–2396, June 2007. doi: 10.1109/ISIE.2007.4374981.

[43] Abir Chatterjee, Ali Keyhani, and Dhruv Kapoor. Identification of photovoltaic source models. *IEEE Transactions on Energy Conversion*, 26(3):883–889, September 2011.

[44] Aissa Chouder, Santiago Silvestre, Nawel Sadaoui, and Lazhar Rahmani. Modeling and simulation of a grid connected pv system based on the evaluation of main pv module parameters. *Simulation Modelling Practice and Theory*, 20:46–58, 2012.

[45] Tao Ma, Hongxing Yang, and Lin Lu. Solar photovoltaic system modeling and performance prediction. *Renewable and Sustainable Energy Reviews*, 36:304–15, 2014.

[46] Marcelo Gradella Villalva, Jonas Rafael Gazoli, and Ernesto Ruppert Filho. Comprehensive approach to modeling and simulation of photovoltaic arrays. *IEEE Transactions on Power Electronics*, 24(5):1198–1208, May 2009.

[47] Luis Castaner and Santiago Silvestre. *Modelling Photovoltaic Systems using PSpice*. John Wiley & Sons Inc., 2002.

[48] Satarupa Bal, Anup Anurag, and B Chitti Babu. Comparative analysis of mathematical modeling of photovoltaic (pv) array. In *India Conference (INDICON), 2012 Annual IEEE*, pages 269–274. IEEE, December 2012.

[49] Yifeng Xie, Jingyu Huang, Xiaokang Liu, Fang Zhuo, Baoquan Liu, and Hailong Zhang. Pv system modeling and a global-planning design for its controller parameters. In *Applied Power Electronics Conference and Exposition (APEC), 2014 Twenty-Ninth Annual IEEE*, pages 3132 – 3135. IEEE, March 2014.

[50] Tao Ma, Hongxing Yang, and Lin Lu. Development of a model to simulate the performance characteristics of crystalline silicon photovoltaic modules/strings/arrays. *Solar Energy*, 100:31 – 41, 2014. ISSN 0038-092X. doi: http://dx.doi.org/10.1016/j.solener.2013.12.003.

[51] A Zeroual, M Raoufi, M Ankrim, and AJ WILKINSON. Design and construction of a closed loop sun-tracker with microprocessor management. *International journal of solar energy*, 19(4):263–274, 1998.

[52] CS Chin, A Babu, and W McBride. Design, modeling and testing of a standalone single axis active solar tracker using matlab/simulink. *Renewable Energy*, 36(11):3075–3090, 2011.

[53] CS Chin. *Model-Based Simulation of an Intelligent Microprocessor-Based Standalone Solar Tracking System.* INTECH Open Access Publisher, 2012.

[54] Pietro P. Altermatt. Models for numerical device simulations of crystalline silicon solar cells—a review. *Journal of Computational Electronics*, 10(3):314–330, 2011. doi: 10.1007/s10825-011-0367-6.

[55] M.A de Blas, J.L Torres, E Prieto, and A GarcÄśÌĄa. Selecting a suitable model for characterizing photovoltaic devices. *Renewable Energy*, 25(3):371 – 380, 2002. ISSN 0960-1481. doi: http://dx.doi.org/10.1016/S0960-1481(01)00056-8.

[56] Ali Naci Celik and NasÄśr Acikgoz. Modelling and experimental verification of the operating current of mono-crystalline photovoltaic modules using four- and five-parameter models. *Applied Energy*, 84(1):1 – 15, 2007. ISSN 0306-2619. doi: http://dx.doi.org/10.1016/j.apenergy.2006.04.007.

[57] Mary D Archer and Robert Hill. *Clean electricity from Photovoltaics.* Imperial College Press, 2001.

[58] Antonio Luque and Steven Hegedus. *Handbook of Photovoltaic Science and Engineering.* John Wiley & Sons Inc., 2nd edition, 2011.

[59] Martin A Green, Keith Emery, Yoshihiro Hishikawa, Wilhelm Warta, and Ewan D Dunlop. Solar cell efficiency tables (version 45). *Progress in Photovoltaics: Research and Applications*, 23:1–9, 2015. doi: http://dx.doi.org/10.1002/pip.2573.

[60] Etienne Saloux, Alberto Teyssedou, and MikhaÃńl Sorin. Explicit model of photovoltaic panels to determine voltages and currents at the maximum power point. *Solar Energy*, 85(5):713 – 722, 2011. ISSN 0038-092X. doi: http://dx.doi.org/10.1016/j.solener.2010.12.022.

[61] Kashif Ishaque, Zainal Salam, Hamed Taheri, and Amir Shamsudin. A critical evaluation of EA computational methods for photovoltaic cell parameter extraction based on two diode model. *Solar Energy*, 85(9):1768 – 1779, 2011. ISSN 0038-092X. doi: http://dx.doi.org/10.1016/j.solener.2011.04.015.

[62] Kashif Ishaque and Zainal Salam. An improved modeling method to determine the model parameters of photovoltaic (pv) modules using differential evolution (de). *Solar Energy*, 85(9):2349 – 2359, 2011. ISSN 0038-092X. doi: http://dx.doi.org/10.1016/j.solener.2011.06.025.

[63] Kashif Ishaque, Zainal Salam, and Hamed Taheri. Simple, fast and accurate two-diode model for photovoltaic modules. *Solar Energy Materials and Solar Cells*, 95(2):586 – 594, 2011. ISSN 0927-0248. doi: http://dx.doi.org/10.1016/j.solmat.2010.09.023.

[64] J A Duffie and W A Beckman. *Solar engineering of thermal processes.* John Wiley & Sons Inc., Hoboken, New Jersey, 3rd edition, 2006.

[65] Sakaros Bogning Dongue, Donatien Njomo, Jean Gaston Tamba, and Lessly Ebengai. Modeling of electrical response of illuminated crystalline photovoltaic modules using four- and five-parameter models. *International Journal of Emerging Technology and Advanced Engineering*, 2(11):612–619, 2012.

[66] R. Chenni, M. Makhlouf, T. Kerbache, and A. Bouzid. A detailed modeling method for photovoltaic cells. *Energy*, 32(9):1724 – 1730, 2007. ISSN 0360-5442. doi: http://dx.doi.org/10.1016/j.energy.2006.12.006.

[67] Vun Jack Chin, Zainal Salam, and Kashif Ishaque. Cell modelling and model parameters estimation techniques for photovoltaic simulator application: A review. *Applied Energy*, 154:500–519, 2015.

[68] Giuseppina Ciulla, Valerio Lo Brano, Vincenzo Di Dio, and Giovanni Cipriani. A comparison of different one-diode models for the representation of iâĂŞv characteristic of a PV cell. *Renewable and Sustainable Energy Reviews*, 32:684 – 696, 2014. ISSN 1364-0321. doi: http://dx.doi.org/10.1016/j.rser.2014.01.027.

[69] Yousef Mahmoud, W Xiao, and H H Zeineldin. A simple approach to modeling and simulation of photovoltaic modules. *Sustainable Energy, IEEE Transactions on*, 3(1):185–186, Jan 2012. ISSN 1949-3029. doi: 10.1109/TSTE.2011.2170776.

[70] Hiren Patel and Vivek Agarwal. Matlab-based modeling to study the effects of partial shading on pv array characteristics. *Energy Conversion, IEEE Transactions on*, 23(1):302–310, March 2008. ISSN 0885-8969. doi: 10.1109/TEC.2007.914308.

[71] Sah Chih-Tang, R N Noyce, and W Shockley. Carrier generation and recombination in p-n junctions and p-n junction characteristics. *Proceedings of the IRE*, 45(9): 1228–1243, Sept 1957. doi: 10.1109/JRPROC.1957.278528.

[72] Keith R McIntosh, Pietro P Altermatt, and Gernot Heiser. Depletion-region recombination in silicon solar cells: when does $m_{DR} = 2$? In *Proceedings of the 16th European photovoltaic solar energy conference*, 2000.

[73] Kensuke Nishioka, Nobuhiro Sakitani, Yukiharu Uraoka, and Takashi Fuyuki. Analysis of multicrystalline silicon solar cells by modified 3-diode equivalent circuit model taking leakage current through periphery into consideration. *Solar Energy Materials and Solar Cells*, 91(13):1222 – 1227, 2007. ISSN 0927-0248. doi: http://dx.doi.org/10.1016/j.solmat.2007.04.009.

[74] Laurence W. Nagel and D.O. Pederson. Spice (simulation program with integrated circuit emphasis). Technical Report UCB/ERL M382, EECS Department, University of California, Berkeley, Apr 1973. URL http://www.eecs.berkeley.edu/Pubs/TechRpts/1973/22871.html.

[75] R Stangl, A Froitzheim, M Schmidt, and W Fuhs. Design criteria for amorphous/crystalline silicon heterojunction solar cells-a simulation study. In *Photovoltaic Energy Conversion, 2003. Proceedings of 3rd World Conference on*, volume 2, pages 1005–1008. IEEE, 2003.

[76] A Froitzheim, R Stangl, L Elstner, M Schmidt, and W Fuhs. Interface recombination in amorphous/crystalline silicon solar cells, a simulation study. In *Photovoltaic*

Specialists Conference, 2002. Conference Record of the Twenty-Ninth IEEE, pages 1238–1241. IEEE, 2002.

[77] R Stangl, A Froitzheim, and W Fuhs. Thin film silicon emitters for crystalline silicon solar cells, epitaxial, amorphous or microcrystalline?-a simulation study. *Proc. PV in Europe, Rome, Italy*, 123, 2002.

[78] Makoto Tanaka, Mikio Taguchi, Takao Matsuyama, Toru Sawada, Shinya Tsuda, Shoichi Nakano, Hiroshi Hanafusa, and Yukinori Kuwano. Development of new a-si/c-si heterojunction solar cells: Acj-hit (artificially constructed junction-heterojunction with intrinsic thin-layer). *Japanese Journal of Applied Physics*, 31 (11R):3518, 1992.

[79] Maarten WM van Cleef, Francisco A Rubinelli, Rita Rizzoli, Roberto Pinghini, Ruud EI Schropp, and Werner F van der Weg. Amorphous silicon carbide/crystalline silicon heterojunction solar cells: a comprehensive study of the photocarrier collection. *Japanese journal of applied physics*, 37(7R):3926, 1998.

[80] AFORS-HET. Automat for simulation of hetero structures, 2016. URL https://www.helmholtz-berlin.de/forschung/oe/ee/si-pv/projekte/asicsi/afors-het/index_en.html.

[81] AMPS-1D. Analysis of microeletronic and photonic structures, 2016. URL http://www.ampsmodeling.org/latest.html.

[82] SCAPS-1D. Solar cell capacitance simulator, 2016. URL http://scaps.elis.ugent.be/.

[83] R. Varache, C. Leendertz, M.E. Gueunier-Farret, J. Haschke, D. MuÃśoz, and L. Korte. Investigation of selective junctions using a newly developed tunnel current model for solar cell applications. *Solar Energy Materials and Solar Cells*, 141:14 – 23, 2015. ISSN 0927-0248. doi: http://dx.doi.org/10.1016/j.solmat.2015.05.014.

[84] Karl W Böer. *Handbook of the Physics of Thin-Film Solar Cells*. Springer Science & Business, 2014.

[85] Chia-Ming Yang, Yuan-Hui Liao, Chun-Hui Chen, Tsung-Cheng Chen, Chao-Sung Lai, and Dorota G. Pijanowska. P-i-n amorphous silicon for thin-film light-addressable potentiometric sensors. *Sensors and Actuators B: Chemical*, pages –, 2016. ISSN 0925-4005. doi: http://dx.doi.org/10.1016/j.snb.2016.04.092.

[86] Yuen Yap Cheng, Burkhard Fückel, Rowan W MacQueen, Tony Khoury, Raphaël GCR Clady, Tim F Schulze, NJ Ekins-Daukes, Maxwell J Crossley, Bernd Stannowski, Klaus Lips, et al. Improving the light-harvesting of amorphous silicon solar cells with photochemical upconversion. *Energy & Environmental Science*, 5 (5):6953–6959, 2012.

[87] Yoshihiro Hamakawa, Funio Koike, and Tetsuya Miyagishi. Color sensor with amorphous pin structure, April 11 1989. US Patent 4,820,915.

[88] B. Mereu, O. Caglar, J.S. Cashmore, P.A. Losio, A. Salabas, and I. Sinicco. Window p-layer in amorphous pin solar cells using zno as transparent conductive oxide. *Solar Energy Materials and Solar Cells*, 152:147 – 154, 2016. ISSN 0927-0248. doi: http://dx.doi.org/10.1016/j.solmat.2016.03.036.

[89] Shuo-Jen Lee, Yi-Ho Chen, Sung-Cheng Hu, Yi-Chung Lin, Jeng-Wei Chang, Tai-Lun Poon, and Wen-Cheng Ke. Improved performance of amorphous si thin-film solar cells on 430 stainless steel substrate by an electrochemical mechanical polishing process. *Journal of Alloys and Compounds*, 558:95 – 98, 2013. ISSN 0925-8388. doi: http://dx.doi.org/10.1016/j.jallcom.2013.01.044.

[90] Paola Delli Veneri, Lucia V Mercaldo, and Iurie Usatii. Silicon oxide based n-doped layer for improved performance of thin film silicon solar cells. *Applied Physics Letters*, 97(2):023512, 2010.

[91] Seung Yeop Myong, Sang Soo Kim, and Koeng Su Lim. Improvement of pin-type amorphous silicon solar cell performance by employing double silicon-carbide pâĂŁ-layer structure. *Journal of Applied Physics*, 95(3):1525–1530, 2004. doi: http://dx.doi.org/10.1063/1.1639140.

[92] R Stangl, A Froitzheim, M Kriegel, T Brammer, S Kirste, L Elstner, H Stiebig, M Schmidt, and W Fuhs. Afors-het, a numerical pc-program for simulation of heterojunction solar cells, version 1.1 (open-source on demand), to be distributed for public use. *Proc. 19th PVSEC, Paris, France*, 1497, 2004.

[93] Pierre Auger. *Sur les rayons [beta] secondaires prodiuts dans un gaz par des rayons x*. Gauthier-Villars, 1925.

[94] We Shockley and WT Read Jr. Statistics of the recombinations of holes and electrons. *Physical review*, 87(5):835, 1952.

[95] Re N Hall. Electron-hole recombination in germanium. *Physical Review*, 87(2): 387, 1952.

[96] Arvind Shah, J. Meier, E. Vallat-Sauvain, C. Droz, U. Kroll, N. Wyrsch, J. Guillet, and U. Graf. Microcrystalline silicon and âĂŸmicromorphâĂŹ tandem solar cells. *Thin Solid Films*, 403âĂŞ404:179 – 187, 2002. ISSN 0040-6090. doi: http://dx.doi.org/10.1016/S0040-6090(01)01658-3. Proceedings of Symposium P on Thin Film Materials for Photovoltaics.

[97] U Kroll, J Meier, L Fesquet, J Steinhauser, S Benagli, JB Orhan, B Wolf, D Borrello, L Castens, Y Djeridane, et al. Recent developments of high-efficiency micromorph tandem solar cells in kai-m/plasmabox pecvd reactors. In *Proc. 26th European Photovoltaic Solar Energy Conf., Hamburg, Germany*, 2011.

[98] J. Meier, U. Kroll, E. Vallat-Sauvain, J. Spitznagel, U. Graf, and A. Shah. Amorphous solar cells, the micromorph concept and the role of vhf-gd deposition technique. *Solar Energy*, 77(6):983 – 993, 2004. ISSN 0038-092X. doi: http://dx.doi.org/10.1016/j.solener.2004.08.026. Thin Film PV.

[99] Sven Burdorf, Gottfried Heinrich Bauer, and Rudolf Brüggemann. Numerical simulations on the limits for the efficiency improvement of hybrid dye-microcrystalline silicon solar cells. *Solar Energy Materials and Solar Cells*, 99:345–348, 2012.

[100] M Nath, S Chakraborty, EV Johnson, A Abramov, P Roca i Cabarrocas, and P Chatterjee. Factors limiting the open-circuit voltage in microcrystalline silicon solar cells. *EPJ Photovoltaics*, 2:20101, 2011.

[101] J Meier, S Dubail, D Fischer, JA Anna Selvan, N Pellaton Vaucher, R Platz, Ch Hof, R Flückiger, U Kroll, N Wyrsch, et al. The" micromorph" solar cells: a new way to high efficiency thin film silicon solar cells. In *13th EC Photovoltaic Solar Energy Conference*, number PV-LAB-CONF-1995-004, pages 1445–1450, 1995.

[102] Lisha Bai, Bofei Liu, Jun Fan, Dekun Zhang, Changchun Wei, Jian Sun, Ying Zhao, and Xiaodan Zhang. The trade-off of light trapping between top and bottom cell in micromorph tandem solar cells with sputtering zno: Al glass substrate. *Journal of Power Sources*, 266:138–144, 2014.

[103] Vladislav Jovanov, Ujwol Planchoke, Philipp Magnus, Helmut Stiebig, and Dietmar Knipp. Influence of back contact morphology on light trapping and plasmonic effects in microcrystalline silicon single junction and micromorph tandem solar cells. *Solar Energy Materials and Solar Cells*, 110:49–57, 2013.

[104] J Krc, K Brecl, F Smole, and M Topic. The effects of enhanced light trapping in tandem micromorph silicon solar cells. *Solar energy materials and solar cells*, 90 (18):3339–3344, 2006.

[105] Julien Bailat, Didier Dominé, R Schluchter, Jérôme Steinhauser, Sylvie Fay, F Freitas, C Bucher, Luc Feitknecht, Xavier Niquille, T Tscharner, et al. High-efficiency pin microcrystalline and micromorph thin film silicon solar cells deposited on lpcvd zno coated glass substrates. In *2006 IEEE 4th World Conference on Photovoltaic Energy Conference*, volume 2, pages 1533–1536. IEEE, 2006.

[106] F-J Haug, T Söderström, M Python, V Terrazzoni-Daudrix, X Niquille, and C Ballif. Development of micromorph tandem solar cells on flexible low-cost plastic substrates. *Solar Energy Materials and Solar Cells*, 93(6):884–887, 2009.

[107] Johannes Meier, Evelyne Vallat-Sauvain, S Dubail, U Kroll, J Dubail, S Golay, Luc Feitknecht, Pedro Torres, Sylvie Fay, D Fischer, et al. Microcrystalline/micromorph silicon thin-film solar cells prepared by vhf-gd technique. *Solar Energy Materials and Solar Cells*, 66(1):73–84, 2001.

[108] Andreas Bielawny, Johannes Üpping, Paul T Miclea, Ralf B Wehrspohn, Carsten Rockstuhl, Falk Lederer, Marius Peters, Lorenz Steidl, Rudolf Zentel, Seung-Mo Lee, et al. 3d photonic crystal intermediate reflector for micromorph thin-film tandem solar cell. *physica status solidi (a)*, 205(12):2796–2810, 2008.

[109] Didier Dominé, Julien Bailat, Jérôme Steinhauser, Arvind Shah, and Christophe Ballif. Micromorph solar cell optimization using a zno layer as intermediate reflector. In *2006 IEEE 4th World Conference on Photovoltaic Energy Conference*, volume 2, pages 1465–1468. IEEE, 2006.

[110] Didier Dominé, Peter Buehlmann, Julien Bailat, Adrian Billet, Andrea Feltrin, and Christophe Ballif. Optical management in high-efficiency thin-film silicon micromorph solar cells with a silicon oxide based intermediate reflector. *physica status solidi (RRL)-Rapid Research Letters*, 2(4):163–165, 2008.

[111] J Krc, F Smole, and M Topic. Optical simulation of the role of reflecting interlayers in tandem micromorph silicon solar cells. *Solar energy materials and solar cells*, 86(4):537–550, 2005.

[112] T Söderström, F-J Haug, X Niquille, V Terrazzoni, and C Ballif. Asymmetric intermediate reflector for tandem micromorph thin film silicon solar cells. *Applied Physics Letters*, 94(6):063501, 2009.

[113] SS Bohra and AK Panchal. Optimization of absorber layers' thickness in a si micromorph solar cell for current matching with intermediate zno reflector. *Journal of Renewable and Sustainable Energy*, 5(2):023121, 2013.

[114] A Čampa, M Meier, M Boccard, LV Mercaldo, M Ghosh, C Zhang, T Merdzhanova, J Krč, F-J Haug, and M Topič. Micromorph silicon solar cell optical performance: Influence of intermediate reflector and front electrode surface texture. *Solar Energy Materials and Solar Cells*, 130:401–409, 2014.

[115] JY Huang, CW Hsu, Jia-Min Shieh, and Peichen Yu. Device modeling of a micromorph tandem solar cell using amps-1d. In *Photovoltaic Specialists Conference (PVSC), 2010 35th IEEE*, pages 001512–001515. IEEE, 2010.